CONFIDENTIAL

Copy 602

NASA TM X-214

(NASA-TM-X-214) FREE-FLIGHT INVESTIGATION OF THE BASE PRESSURE AND DRAG OF A FLARE-STABILIZED BLUNT-NOSE REENTRY BODY HAVING A FINENESS RATIO OF 3.11 AT MACH R.J. Mayhue, et al (NASA) Mar. 1960 40 p 00/99 N72-71145 Unclas 21337

NASA TM X-214

TECHNICAL MEMORANDUM

X-214

CLASSIFICATION CHANGED
UNCLASSIFIED
TO
By Authority of T.D. 72-136 Date 3-21-72

FREE-FLIGHT INVESTIGATION OF THE BASE PRESSURE AND DRAG OF A FLARE-STABILIZED BLUNT-NOSE REENTRY BODY HAVING A FINENESS RATIO OF 3.11 AT MACH NUMBERS FROM 0.70 TO 1.90

By Robert J. Mayhue and Willard S. Blanchard, Jr.

Langley Research Center
Langley Field, Va.

CATEGORY

FACILITY FORM 602

(ACCESSION NUMBER) 40 (PAGES) (NASA CR OR TMX OR AD NUMBER)

(THRU) None (CODE) (CATEGORY)

NATIONAL AERONAUTICS AND SPACE ADMINISTRATION

WASHINGTON

March 1960

CONFIDENTIAL

CONFIDENTIAL

NATIONAL AERONAUTICS AND SPACE ADMINISTRATION

TECHNICAL MEMORANDUM X-214

FREE-FLIGHT INVESTIGATION OF THE BASE PRESSURE AND DRAG OF A FLARE-STABILIZED BLUNT-NOSE REENTRY BODY HAVING A FINENESS RATIO OF 3.11 AT MACH NUMBERS FROM 0.70 TO 1.90*

By Robert J. Mayhue and Willard S. Blanchard, Jr.

SUMMARY

Free-flight tests have been conducted to determine the base pressures and drag of a flare-stabilized blunt-nose reentry body having a fineness ratio of 3.11. Two models were tested with center-of-gravity locations at 42.0 percent and 38.9 percent of the body length through a Mach number range from 0.70 to 1.90 and a Reynolds number range from 1.30×10^6 to 6.55×10^6, based on body cylinder diameter.

High amplitude, nonplanar oscillations of the model at the transonic and subsonic speeds resulted in a large spread in the values of the base pressure coefficients. In general, the average of the pressure coefficients over the base became more negative with increasing angle of attack and showed a tendency to level off at the higher angles of attack at the higher Mach numbers. High amplitude oscillations of the model at the transonic and subsonic speeds also resulted in an increase in the average total drag coefficient averaging approximately 20 percent over the total drag coefficient at the zero-lift condition. The base drag constituted between 40 to 50 percent of the total drag at the transonic and subsonic speeds. The amplitude of the oscillations was considerably reduced and delayed to a lower Mach number when the center of gravity of the model was moved forward from 42.0 percent to 38.9 percent of the body length. Based on the results of wind-tunnel tests on similar models, the difference in oscillation characteristics of the two models can be attributed to the change in the static margin resulting from both lower flight test Reynolds numbers and more forward center-of-gravity position for one of the models.

---

*Title, Unclassified.

CONFIDENTIAL

CONFIDENTIAL

INTRODUCTION

A general research program is being conducted by the Pilotless Aircraft Research Division of the Langley Research Center to determine the performance characteristics of bluff body shapes by means of the rocket-boosted free-flight model technique. References 1 and 2 present free-flight force measurements for similar flare-stabilized blunt-body configurations at Mach numbers up to 2.8 and 10.15, respectively. Reference 2 also presents aerodynamic-heating data obtained during large oscillations of the model. Force and stability data for flare-stabilized bodies and for low-fineness-ratio right-circular cylinders are presented in references 3 and 4 for Mach numbers up to 2.15.

L 6 5 6

This paper presents the results of a base pressure and drag investigation of a reentry body consisting of a blunt-nose cylinder with a cone-frustum afterbody. A qualitative discussion of the model motions at the transonic and subsonic speeds is also included. Two models, similar except for instrumentation and center-of-gravity location, were flight tested at the NASA Wallops Station. The tests covered a Mach number range from 0.70 to 1.90 and a Reynolds number range from 1.3×10^6 to 6.55×10^6, based on the body cylinder diameter.

SYMBOLS

A_B base annular area, sq ft

a accelerometer reading, g units

C_A longitudinal-force coefficient, $-a_l \frac{W}{qS}$

C_D drag coefficient, based on reference area 0.454 sq ft

$C_{D,B}$ base drag coefficient, $-C_p \frac{S_B}{S}$

$C_{D,T}$ total drag coefficient, $C_A \cos \alpha_R + C_R \sin \alpha_R$

C_N normal-force coefficient, $a_n \frac{W}{qS}$

C_R resultant-force coefficient (always plotted as a positive number), $\sqrt{C_N^2 + C_Y^2}$

CONFIDENTIAL

C_Y transverse-force coefficient, $a_t \frac{W}{qS}$

C_p base pressure coefficient, $\frac{p_b - p_\infty}{q}$

$\overline{C}_p$ weighted average base pressure coefficient, $\sum C_p \frac{A_B}{S_B}$

I moment of inertia in pitch or yaw, slug-ft^2

I_X moment of inertia in roll, slug-ft^2

K nose reentry parameter, $\frac{C_D S}{m \sin \xi}$

M Mach number

m mass, slugs

n fineness ratio, $\frac{\text{Length}}{\text{Cylinder diameter}}$

P pressure orifice

p rate of roll, $\frac{\Delta\Lambda - \pi}{\Delta t\left(\frac{I_X}{2I} - 1\right)}$, radians/sec; pressure, lb/sq ft

q free-stream dynamic pressure, lb/sq ft

R Reynolds number, based on cylinder diameter

S reference area based on the cross-sectional area of body cylinder (0.454 sq ft)

S_B base area, sq ft

t time, sec

V velocity, ft/sec

W weight, lb

α_R resultant angle of attack

$\dot{\theta}$ angular velocity in pitch, radians/sec

Λ angular orientation of resultant vector, radians

ξ reentry angle, radians

$\dot{\psi}$ angular velocity in yaw, radians/sec

Subscripts:

B base

l longitudinal

m manifold

n normal

t transverse

∞ free stream

1,2,3,4, and 5 base-pressure orifice designation

L 6 5 6

MODELS

The external shape and general dimensions of the models tested are presented in figure 1. The models were constructed of stainless steel and consisted of a blunt nose, a cylindrical center section, and a 16.5° cone-frustum afterbody. The nose shape of the models was defined by the reentry parameter $K = 0.16$ and by the coordinates derived from the following equation:

$$\left(\frac{Y}{4.56}\right)^{2} + \left(\frac{2.28 - X}{2.28}\right)^{2.5} = 1.0$$

The length-to-cylinder-radius ratio of the nose was 0.50. Both models had a fineness ratio of 3.11 and were similar except for center-of-gravity locations. A comparison of the mass characteristics of the models is presented in table I. The first model tested, designated as model A, had a center-of-gravity location at 42.0 percent of the body length. The second model, designated as model B, had a more forward center of gravity located at 38.9 percent of the body length. The base

of the afterbody was sealed with a backplate having a spherical curvature defined by the coordinates given in the table of figure 1. Fixtures were attached to the base of the models to simulate reentry attitude pulse-jet controls. A photograph of the model is presented as figure 2.

TEST AND INSTRUMENTATION

A photograph showing model A and booster in the launching position is presented as figure 3. The booster for model A consisted of a solid-propellant Cajun rocket motor with fins for stabilization and a 20° flare to provide a drag separation force at burnout of the booster. The model was launched at an angle of approximately 75° and was accelerated to a maximum Mach number of about 1.22. The Reynolds number varied from 3.41×10^6 at $M = 0.70$ to 6.55×10^6 at $M = 1.20$ for model A.

A photograph showing model B and two-stage booster system in the launching position is presented as figure 4. The booster arrangement for model B consisted of a first-stage solid-propellant Nike rocket motor with fins for stabilization and a second-stage Cajun booster system similar to that used for model A. Model B was launched at an angle of approximately 75° and was accelerated to a maximum Mach number of about 2.0 by the second-stage Cajun booster. Separation of the model occurred shortly after the second boost peak Mach number was reached. The flight test Reynolds number varied from 1.30×10^6 at $M = 0.70$ to 5.02×10^6 at $M = 1.9$ for model B. Figure 5 presents the variation of Reynolds number with Mach number for both models.

A 10-channel telemeter was carried in each of the models and continuously transmitted measurements of normal, transverse, and longitudinal accelerations, total pressure at the nose, base pressures, rate of pitch, and rate of yaw. Pressures over the base were measured at the locations shown in figure 6. It should be noted that rate of pitch and rate of yaw were measured for model B only.

Ground instrumentation included a CW Doppler radar unit to measure the velocity of the model and NASA modified SCR-584 tracking radar to determine the flight path. Atmospheric data were obtained from a rawinsonde released from the ground immediately before launching of the model.

CONFIDENTIAL

DATA REDUCTION

All the data were recorded and analyzed during coasting flight as the models, separated from their boosters, decelerated through the Mach number range reported. The measured quantities were reduced to coefficient form as defined in the section "Symbols." The CW Doppler radar measurements used to determine the average total drag coefficients were corrected for flight path angle and winds aloft.

The rate of roll was estimated by using the method of reference 5 and the following equation:

$$p = \frac{\Delta\Lambda - \pi}{\Delta t\left(\frac{I_X}{2I} - 1\right)}$$

Values for the resultant angles of attack presented herein were estimated from test results on similar models obtained at the Ames 6- by 6-foot supersonic tunnel. The angle of attack was taken at values of wind-tunnel normal-force coefficients corresponding to the resultant-force coefficients measured for the models of these tests, the resultant-force coefficient being assumed approximately equal to the normal-force coefficient.

ACCURACY

Estimated maximum experimental errors are given in the following table in coefficient form for models A and B at several representative Mach numbers. The Mach number is estimated to be accurate within ±0.01 over the range of Mach numbers indicated. Based on the scatter of data points, the random errors are believed to be much smaller than the magnitudes of the errors stated in the following table:

Coefficient	Model A			Model B		
	Mach number			Mach number		
	1.20	0.90	0.70	1.90	1.30	0.70
C_A	±0.11	±0.20	±0.32	±0.11	±0.25	±0.91
C_N	±.08	±.15	±.28	±.06	±.16	±.76
C_Y	±.08	±.16	±.25	±.06	±.16	±.70
C_p	±.03	±.05	±.12	±.01	±.03	±.19

CONFIDENTIAL

It should be noted that the existence of isolated scatter of data points in the time histories presented in figures 7 and 8 gives no indication of the accuracy of the data. The time histories are made up of machine plotted points taken from magnetic tape recordings and include some points which were affected by signal noises inadvertently picked up by the ground receiving station. Such points are not considered in either the analysis of the data or in the estimation of the data accuracies.

RESULTS AND DISCUSSION

Model Motions

Since the primary data for the flight tests of models A and B were base pressures and drag, analysis of the model motions is limited to a qualitative discussion of the measured results. An indication of the motions of models A and B may be seen in the time histories presented in figures 7 and 8 and in the cross plots of C_N and C_Y presented in figures 9 and 10. It should be noted that the resultant-force coefficients are always plotted as a positive number in the time histories.

As shown in figure 7, model A deviated from the zero-lift condition shortly after separation at Mach number 1.2 with a buildup in the resultant-force coefficient. The corresponding resultant angle of attack prior to the initiation of the nonplanar oscillations at Mach number 1.05 was approximately 8°. The amplitude of the oscillations increased to a maximum of about $\pm 24^\circ$ at Mach number 0.98. Large amplitude oscillations about a trim were sustained throughout the remaining decelerating portion of the flight with a slight tendency to damp at the subsonic speeds as shown in figures 7 and 9. In comparison, model B with the center of gravity moved forward to the 38.9-percent station and at a lower flight test Reynolds number flew an essentially zero-lift trajectory through the supersonic speed range. Nonplanar oscillations did not occur for this model until a lower decelerating Mach number of 0.86 was reached. The buildup in resultant angle of attack before the start of the oscillations of model B was limited to approximately 2°. Undamped oscillations of about $\pm 6^\circ$ were sustained throughout the remaining subsonic portion of the flight as indicated in figures 8 and 10.

The occurrence of large pitching oscillations at the transonic speeds noted here for model A may be explained by the wind-tunnel results of references 6 and 7 obtained in the Ames 6- by 6-foot supersonic tunnel and in the 11- by 11-foot transonic test section of the Ames Unitary Plan wind tunnel. Reference 6 shows that hysteresis loops were present

CONFIDENTIAL

in the pitching-moment curves as the result of separation and reattachment of the flow during increasing and decreasing angle-of-attack cycles of the body. The energy input represented by the hysteresis loops in the pitching-moment curves resulted in the increased oscillation amplitudes experienced by model A between Mach numbers 1.05 and 0.98. Reference 6 shows that the oscillation amplitudes reach a limit cycle when the energy imparted by the hysteresis loops is absorbed by the stable pitch damping of the model. Analog computer studies of reference 7 show that the limit-cycle oscillations for a model similar to model A was approximately ±25° which is in good agreement with the values given for model A.

L 6 5 6

The considerable difference noted between the amplitude of the oscillations of models A and B may also be explained by the results of references 6 and 7. Model A, with the center of gravity at the 42.0-percent station, was neutrally stable at the higher Reynolds number and at Mach numbers greater than 1.0 allowing a deflection up to the angle of attack for flow separation. The hysteresis loops present in the pitching-moment curves then produced the large amplitude limit-cycle oscillations exhibited by model A. On the other hand, model B with a more forward center-of-gravity location and lower flight test Reynolds number did not attain an angle of attack large enough for separation to occur while decelerating through the supersonic and transonic speeds. At the subsonic Mach numbers, wind-tunnel results of reference 6 show that separation occurs around the entire nose of the model resulting in unstable damping in pitch at angles of attack near zero. Since the pitch damping of the model was stable at higher angles of attack, a limit-cycle oscillation developed although of smaller amplitude than those produced by the hysteresis loop. Unpublished results of a similar model fired in the Ames supersonic free-flight wind tunnel at subsonic speeds developed a limit-cycle oscillation of from ±6° to ±8° amplitude, which is in good agreement with the amplitudes shown for model B at the subsonic speeds.

Since instrumentation was not provided in either of the models to measure roll rates, the method of reference 5 was used to estimate the rate of roll of model A from the cross plot of C_N and C_Y presented in figure 9. Assuming a constant trim center at $C_N = 0.18$ and $C_Y = 0.14$, the estimated rate of roll of model A varied between 2.25 and 4.25 radians per second. The rate of roll of model B was difficult to obtain by the method of reference 5 because of the circular motion of the C_N and C_Y plots about a trim center that appeared to vary both in magnitude and direction (fig. 10). Results obtained in the Langley 16-foot transonic tunnel during transonic and subsonic tests of a blunt-nose flare-stabilized body similar to the configuration of this investigation show that the variation of base pressure coefficients

CONFIDENTIAL

with roll was small with roll rates up to 38 radians per second and angles of attack up to 15°. It is believed, then, that the rolling motions of models A and B had little effect on the measured values of pressure and force coefficients.

Base Pressures

The variation of the base pressure coefficients with Mach number is presented in figure 11 for the flight test Mach number range of models A and B. Good agreement was obtained between the individual base pressure measurements of the two models near the zero-lift condition between M = 1.1 and M = 1.2. At the lower Mach numbers, however, a large difference between the base pressure coefficients of the two models was evident. Figures 7 and 8 show that the base pressure coefficients of models A and B oscillated in phase and at the same frequencies as the resultant-force coefficients during the sustained oscillations at the transonic and subsonic speeds. The difference in the base pressure coefficients between models A and B as shown in figure 11 can therefore be partially attributed to the difference between the angle-of-attack oscillations of the two models. In addition, the difference in the orientation of the base pressure orifices with respect to the instantaneous plane of oscillation and the difference in Reynolds number of the two models is probably reflected in the large difference in the base pressure coefficients at the transonic and subsonic speeds. It should also be noted that larger experimental errors in the base pressure measurements are possible at the lower Mach numbers. The envelope of the base pressure coefficients obtained for models A and B are shown in figure 12 for the flight test Mach number range of each model. The range of base pressure coefficients during the oscillations of the models at the transonic and subsonic speeds correspond to a resultant angle-of-attack maximum variation of ±24° for model A and ±6° for model B. It is interesting to note that the envelope of the base pressure coefficients was small for the approximately zero-lift condition at the supersonic speeds.

Figure 13 presents the variation of the base pressure coefficients of models A and B with Mach number at approximately zero angle of attack. The data points shown in figures 13(a) and 13(b) correspond to resultant angles of attack of less than 2°. The solid-line curves in figures 13(a) and 13(b) represent the weighted average of the individual measurements of base pressure coefficients of model A and model B at approximately zero angle of attack. Figure 13(c) presents the variation of the average base pressure coefficient with Mach number for both models A and B at approximately zero angle of attack.

The variation of the average of the pressure coefficients over the base with resultant angle of attack is presented in figure 14 for

model A during several half-cycle oscillations at the transonic and subsonic speeds. A hysteresis effect on the base pressure coefficients was noted during the increasing and decreasing angle-of-attack oscillations. The hysteresis effect became less pronounced with decreasing Mach number, however, and the base pressure coefficients at the increasing angle-of-attack portion of the cycle were essentially the same at the corresponding angles during the decreasing angles of attack. Results obtained in the Langley 16-foot transonic tunnel for a similar blunt-nose reentry body with a 10° flare angle and a fineness ratio of 3.79 are also shown in figure 14 to substantiate the trend of the changes in base pressure coefficients with angle of attack for the configuration of this investigation. The base pressures measured on the wind-tunnel model correspond to the manifold base pressures of models A and B. Although there is no agreement between the magnitudes of the base pressure coefficients or between the variation of the base pressure coefficients with Mach number at the same angle of attack, the manner in which the base pressure coefficients vary with angle of attack is similar for both the free-flight and wind-tunnel tests. Reference 8 presents additional base pressure data from tests in the Ames 6- by 6-foot supersonic tunnel of similar models. These tests also show similar variations of the base pressure coefficients with angle of attack. It should be noted in figure 14 that the base pressure coefficients show a tendency to level off at the higher angles of attack and at the higher Mach numbers for both the free-flight and wind-tunnel configurations.

L 6 5 6

DRAG

The variation of the total and base drag coefficient with Mach number at approximately zero angle of attack is presented in figure 15 for both models A and B. The data points shown in figure 15(a) for the total drag coefficients as determined from accelerometer measurements correspond to resultant angles of attack of less than 2°. The maximum value of total drag coefficient appeared to occur at approximately $M = 1.1$ and was taken as $C_D = 1.97$ for both models A and B. The base drag coefficient at approximately zero angle of attack as shown in figure 15(b) was calculated from the weighted averages of the base pressure coefficients presented in figure 13(c). It is apparent from figure 15 that the base drag of models A and B constitutes a large percentage (40 to 50 percent) of the total drag at the transonic and subsonic speeds.

The total drag coefficient is plotted against resultant angle of attack in figure 16 for several half-cycle oscillations of model A at the transonic and subsonic speeds. The curves shown in figure 16 represent an average value for the total drag coefficient during

oscillations of the model through an increasing and decreasing resultant angle-of-attack range.

The total drag coefficients at approximately zero angle of attack as determined from accelerometer measurements are compared in figure 17 with the average total drag of models A and B computed from CW Doppler radar measurements. Good agreement is shown between the drag measurements for model B at the higher supersonic speeds. A comparison of the drag coefficients could not be made below $M = 1.28$ for model B because of the difficulty in obtaining accurate CW Doppler radar measurements during this portion of the trajectory of model B. The average of the total drag coefficients during the high amplitude oscillations of model A is also shown by CW Doppler radar data points in figure 17. The increase in the average total drag coefficient during the high amplitude oscillations of model A averaged approximately 20 percent over the total drag coefficient at the zero-lift condition.

SUMMARY OF RESULTS

A free-flight investigation was conducted to determine the base pressures and drag of a flare-stabilized blunt-nose reentry body having a nose reentry parameter $K = 0.16$ and an overall fineness ratio of 3.11. Two models were tested with center-of-gravity locations at 42.0 percent and 38.9 percent of the body length. The tests covered a Mach number range from 0.70 to 1.90 and a Reynolds number range from 1.30×10^6 to 6.55×10^6, based on body cylinder diameter. A summary of the results of this investigation is listed as follows:

1. High amplitude oscillations of the model at the transonic and subsonic speeds resulted in a large spread in the values of the base pressure coefficients. In general, the average of the pressure coefficients over the base became more negative with increasing angle of attack with a tendency to level off at the higher angles of attack at the higher Mach numbers.

2. The maximum value of the total drag coefficient at zero angle of attack occurred near a Mach number of 1.1 and reached a value of approximately 1.97. The base drag constituted between 40 to 50 percent of the total drag at the transonic and subsonic speeds.

3. High amplitude oscillations of the model with the rearward center of gravity resulted in an increase in the total drag coefficient averaging about 20 percent over the zero-lift total drag coefficients at the transonic and subsonic speeds.

CONFIDENTIAL

4. High amplitude, nonplanar oscillations were experienced by the model with the center of gravity at 42.0 percent of the body length at the transonic and subsonic speeds but were considerably reduced and delayed to a lower Mach number when the center of gravity was moved forward to 38.9 percent of the body length. Based on the results of wind-tunnel tests on similar models, the difference in the oscillation characteristics of the two models can be attributed to the change in the static margin resulting from both lower flight test Reynolds numbers and more forward center-of-gravity position for one of the models.

Langley Research Center,
National Aeronautics and Space Administration,
Langley Field, Va., October 30, 1959.

L
6
5
6

CONFIDENTIAL

REFERENCES

1. McFall, John C., Jr.: Drag Measurements of a Reentry Body With Rocket-Boosted Models in Free Flight at Mach Numbers From 2.8 to 0.6. NASA TM X-1, 1959.

2. Hall, James R., and Graham, John B., Jr.: Aerodynamic Heating and Lateral Force Measurements of a Blunt-Nose Flare-Cylinder Configuration Undergoing Large Lateral Oscillations at Mach Numbers up to 10.15. NASA TM X-45, 1959.

3. Coltrane, Lucille C.: Stability Investigation of a Blunt Cone and a Blunt Cylinder With a Square Base at Mach Numbers From 0.64 to 2.14. NACA RM L58G24, 1958.

4. Coltrane, Lucille C.: Investigation of Two Bluff Shapes in Axial Free Flight Over a Mach Number Range From 0.35 to 2.15. NACA RM L58A16, 1958.

5. Nelson, Robert L.: The Motions of Rolling Symmetrical Missiles Referred to a Body-Axis System. NACA TN 3737, 1956.

6. Reese, David E., Jr., and Wehrend, William R., Jr.: An Investigation of the Static and Dynamic Aerodynamic Characteristics of a Series of Blunt-Nosed Cylinder-Flare Models at Mach Numbers From 0.65 to 2.20. NASA TM X-110, 1960.

7. Tunnell, Phillips J., Marker, Ralph D., and Reese, David E., Jr.: Characteristics of a Blunt-Nosed Cylindrical Flared Body in Pitch at Transonic Mach Numbers. NASA TM X-159, 1960.

8. Reese, David E., Jr., and Wehrend, William R., Jr.: Effects of Sting-Support Interference on the Base Pressures of a Model Having a Blunt-Nosed Cylinder Body and a Conical Flare at Mach Numbers of 0.65 to 2.20. NASA TM X-161, 1960.

CONFIDENTIAL

L 6 5 6

TABLE I

MODEL MASS CHARACTERISTICS

Characteristic	Model A	Model B
Weight, lb	216.0	204.0
I, slug-ft^2	4.50	4.13
I_X, slug-ft^2	0.55	0.46
Center of gravity, percent body length	42.0	38.9

CONFIDENTIAL

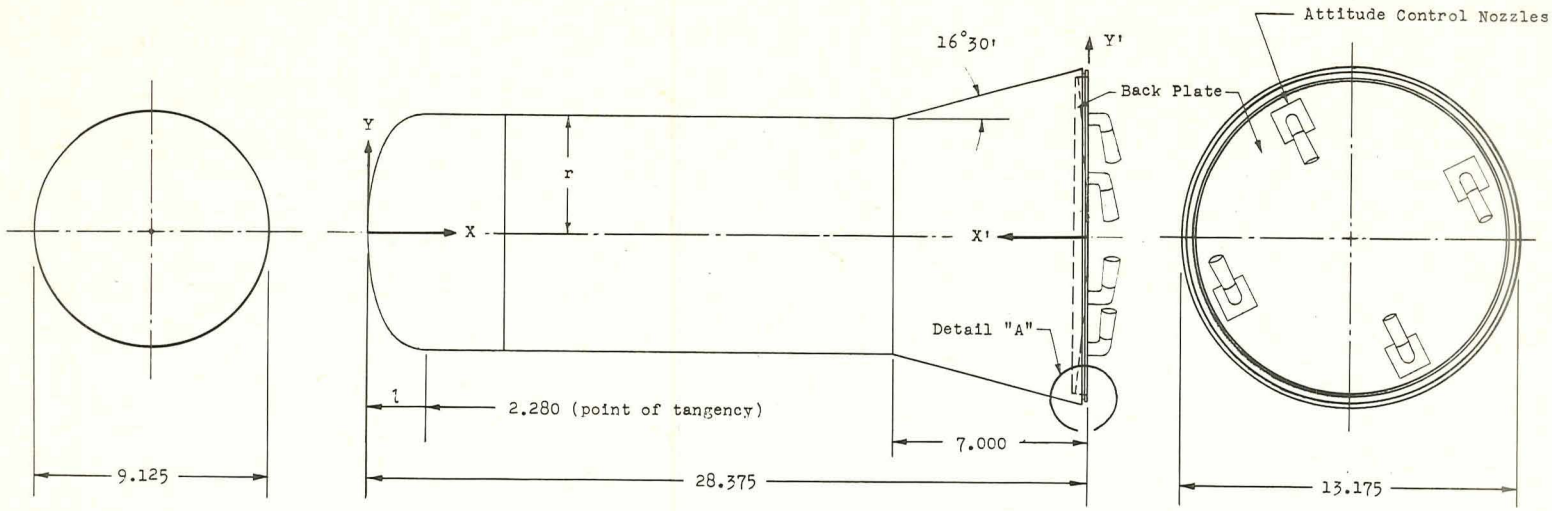

NOSE COORDINATES	
X	Y
0	0
.125	1.670
.250	2.300
.375	2.750
.500	3.100
.750	3.620
1.000	3.990
1.250	4.210
1.500	4.400
1.750	4.500
2.000	4.550
2.280	4.560

BACK PLATE COORDINATES	
X'	Y'
.0005	.500
.005	1.000
.030	1.500
.050	2.000
.070	2.500
.105	3.000
.140	3.500
.195	4.000
.250	4.500
.305	5.000
.370	5.500
.440	6.000
.500	6.300

Model Physical Characteristics

Fineness Ratio 3.11

Base Frontal Area ... 0.947 Ft^2

Body Frontal Area ... 0.454 Ft^2

Nose $\frac{l}{r}$ ... 0.50

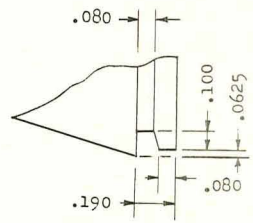

Detail "A"

Figure 1.- General dimensions of models A and B. All dimensions are in inches.

CONFIDENTIAL

CONFIDENTIAL

CONFIDENTIAL

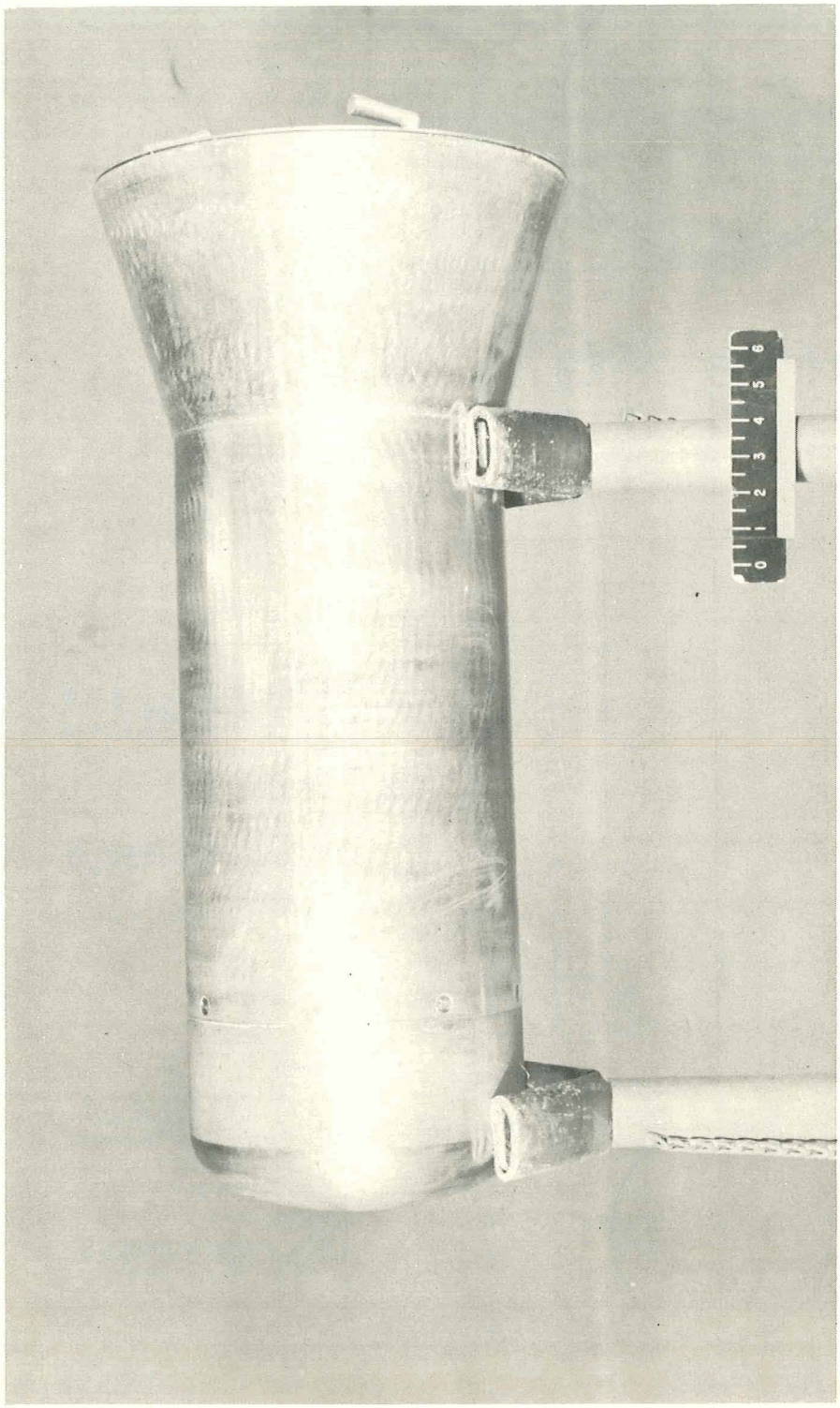

Figure 2.- Photograph of model tested. L-58-669

CONFIDENTIAL

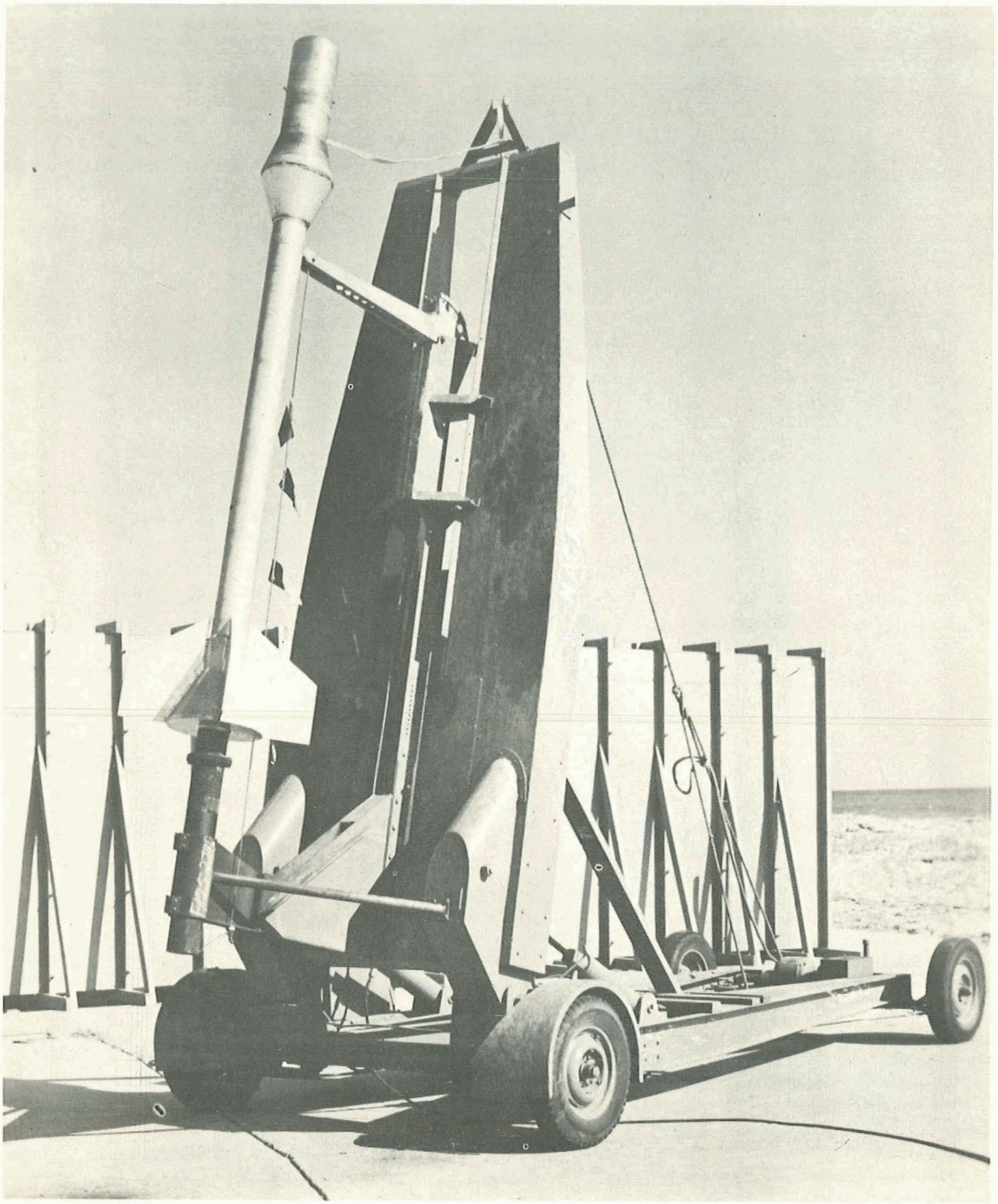

Figure 3.- Photograph of model A and booster on launcher. L-58-1073

CONFIDENTIAL

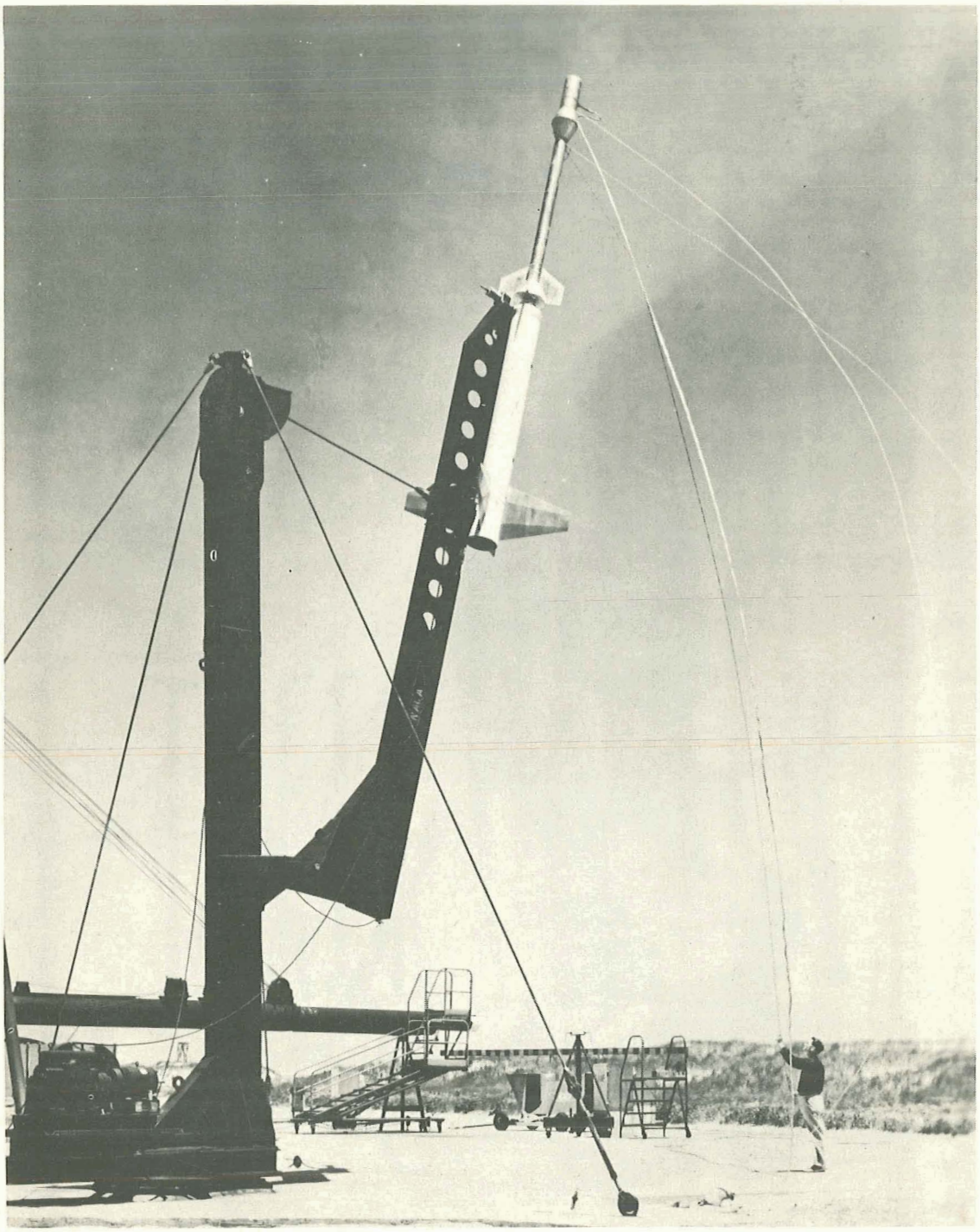

L-656

Figure 4.- Photograph of model B and booster on launcher. L-58-2659

CONFIDENTIAL

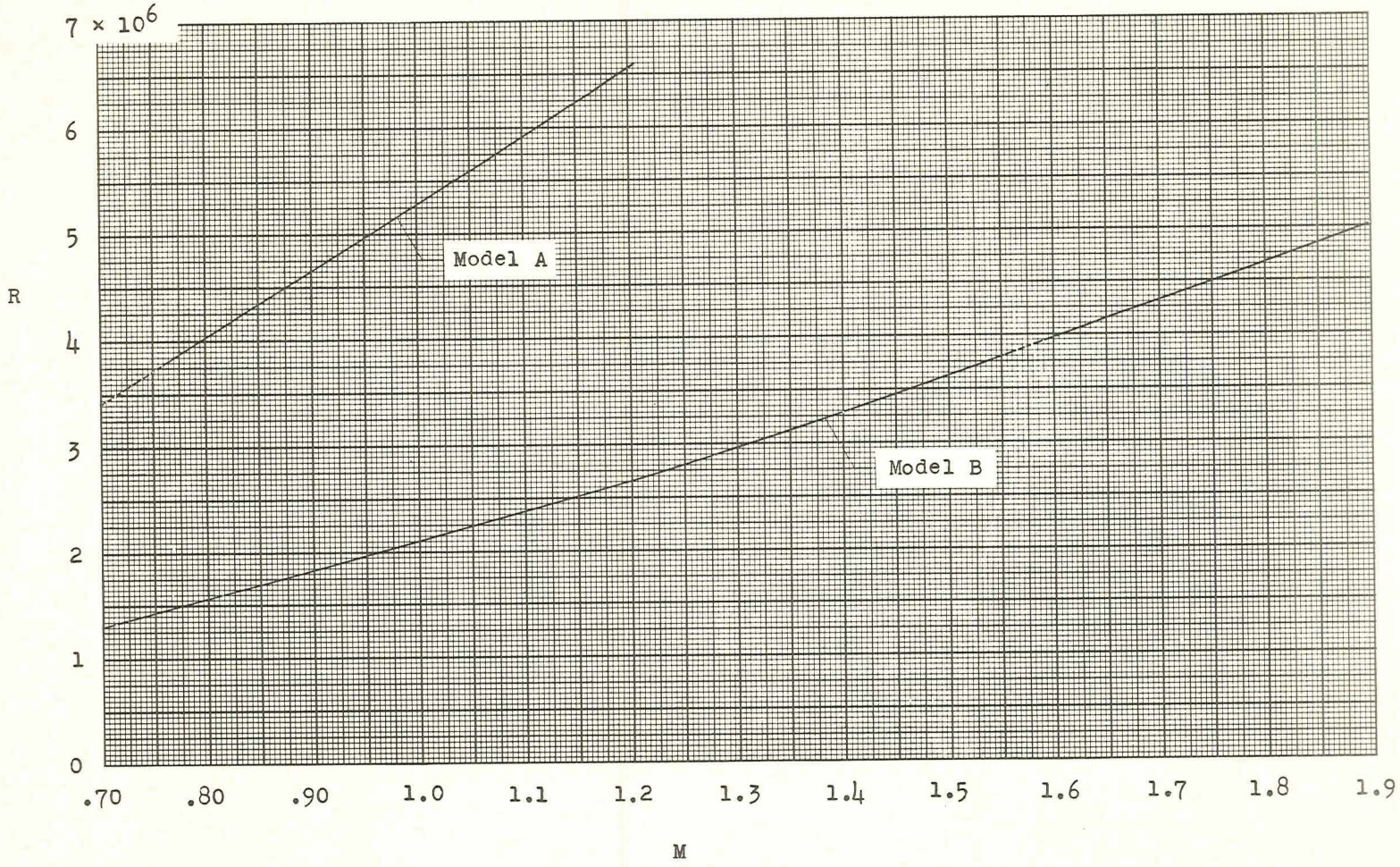

Figure 5.- Variation of flight test Reynolds number with Mach number for models A and B. Reynolds number is based on the model cylinder diameter.

CONFIDENTIAL

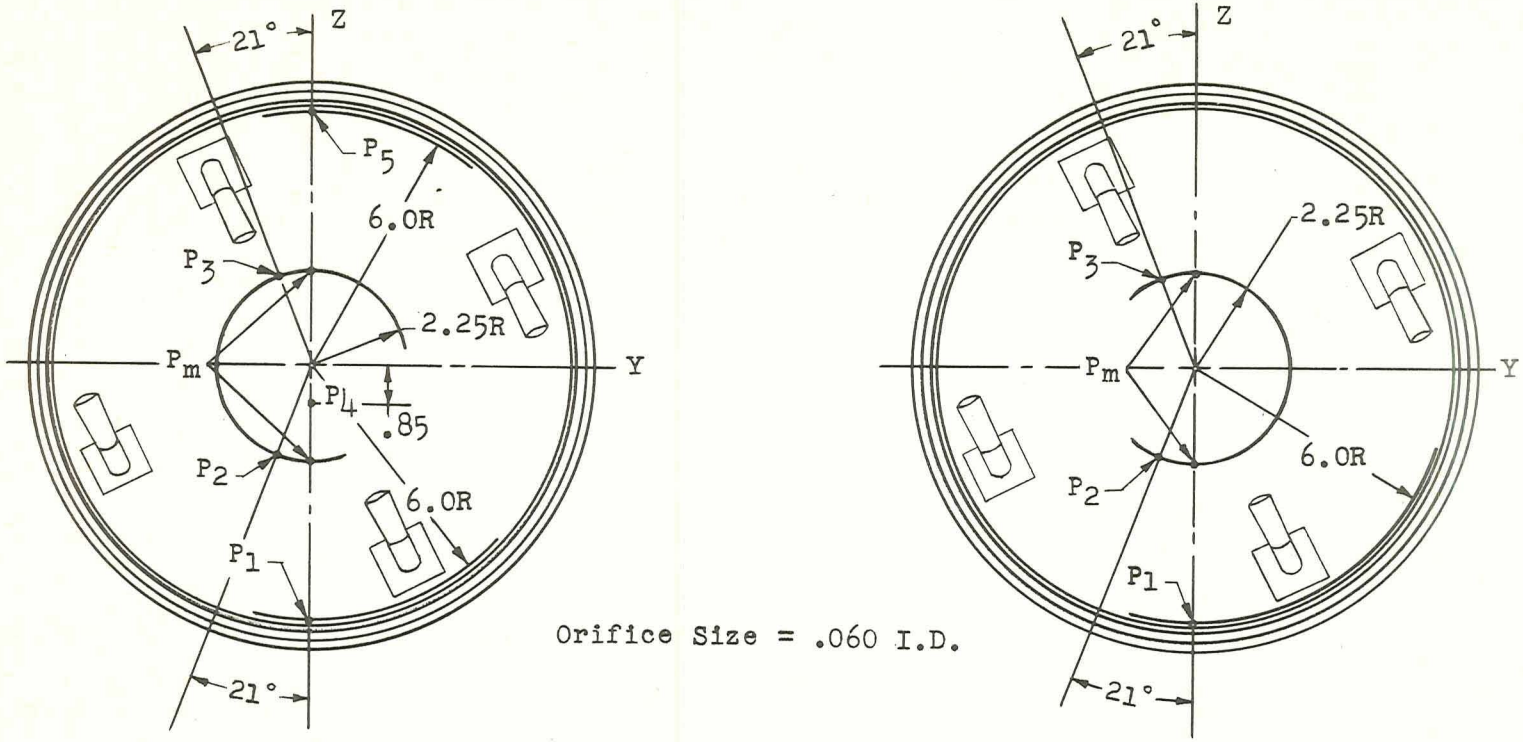

Orifice Size = .060 I.D.

Model A

Model B

Figure 6.- Location of the base-pressure orifices for models A and B. All dimensions are in inches.

CONFIDENTIAL

CONFIDENTIAL

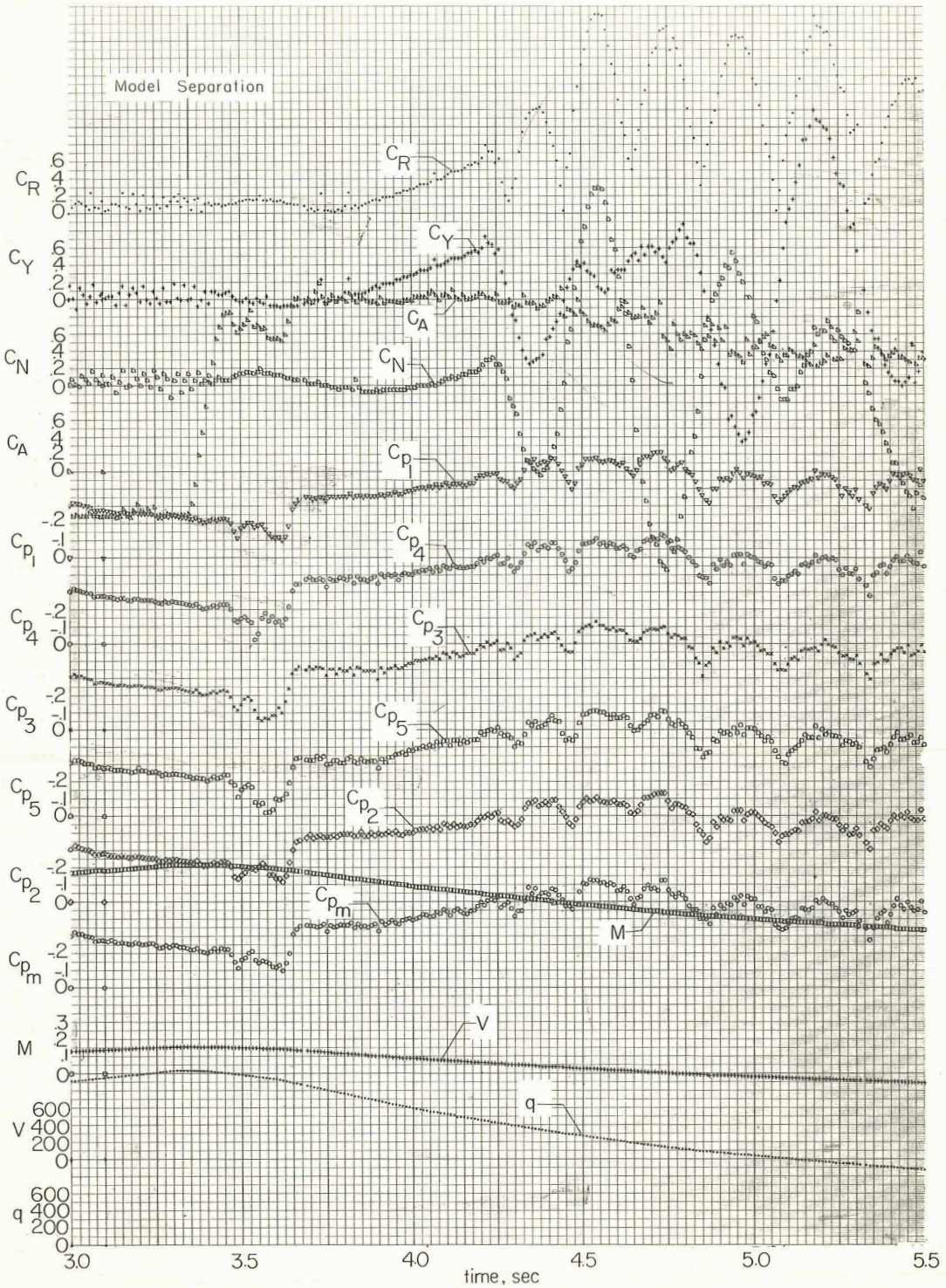

Figure 7.- Time history of free-flight data for model A.

CONFIDENTIAL

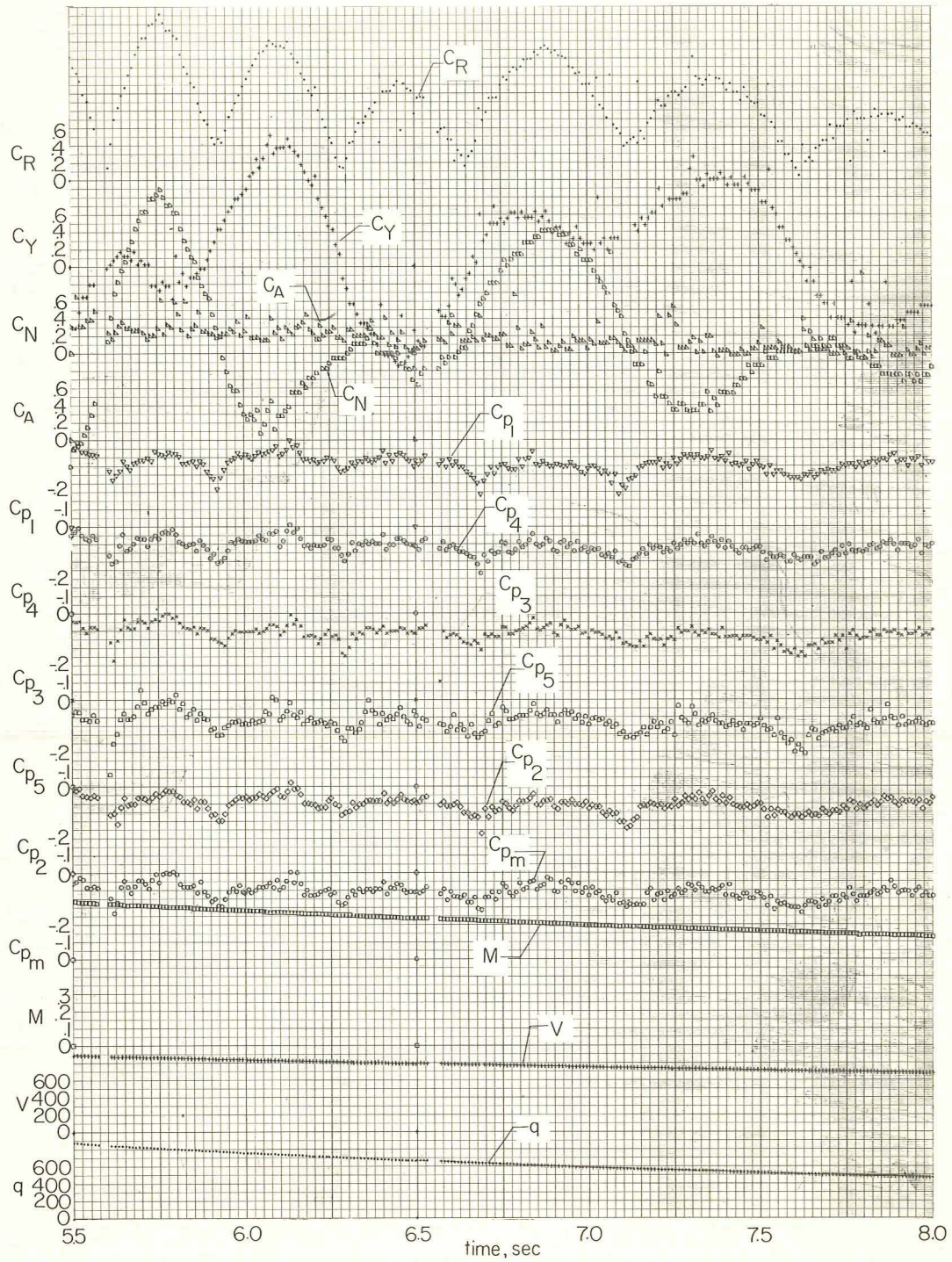

Figure 7.- Continued.

CONFIDENTIAL

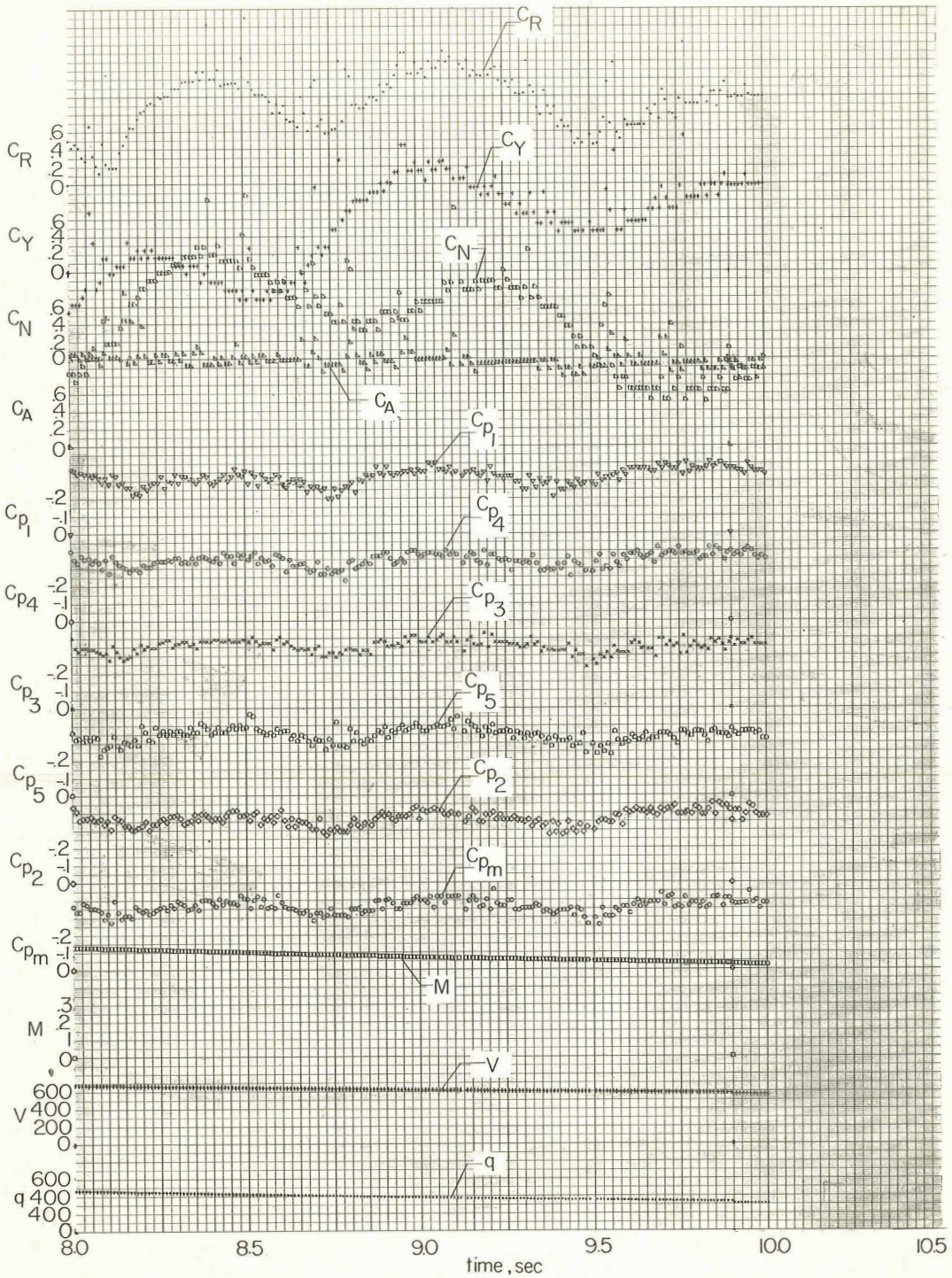

Figure 7.- Concluded.

CONFIDENTIAL

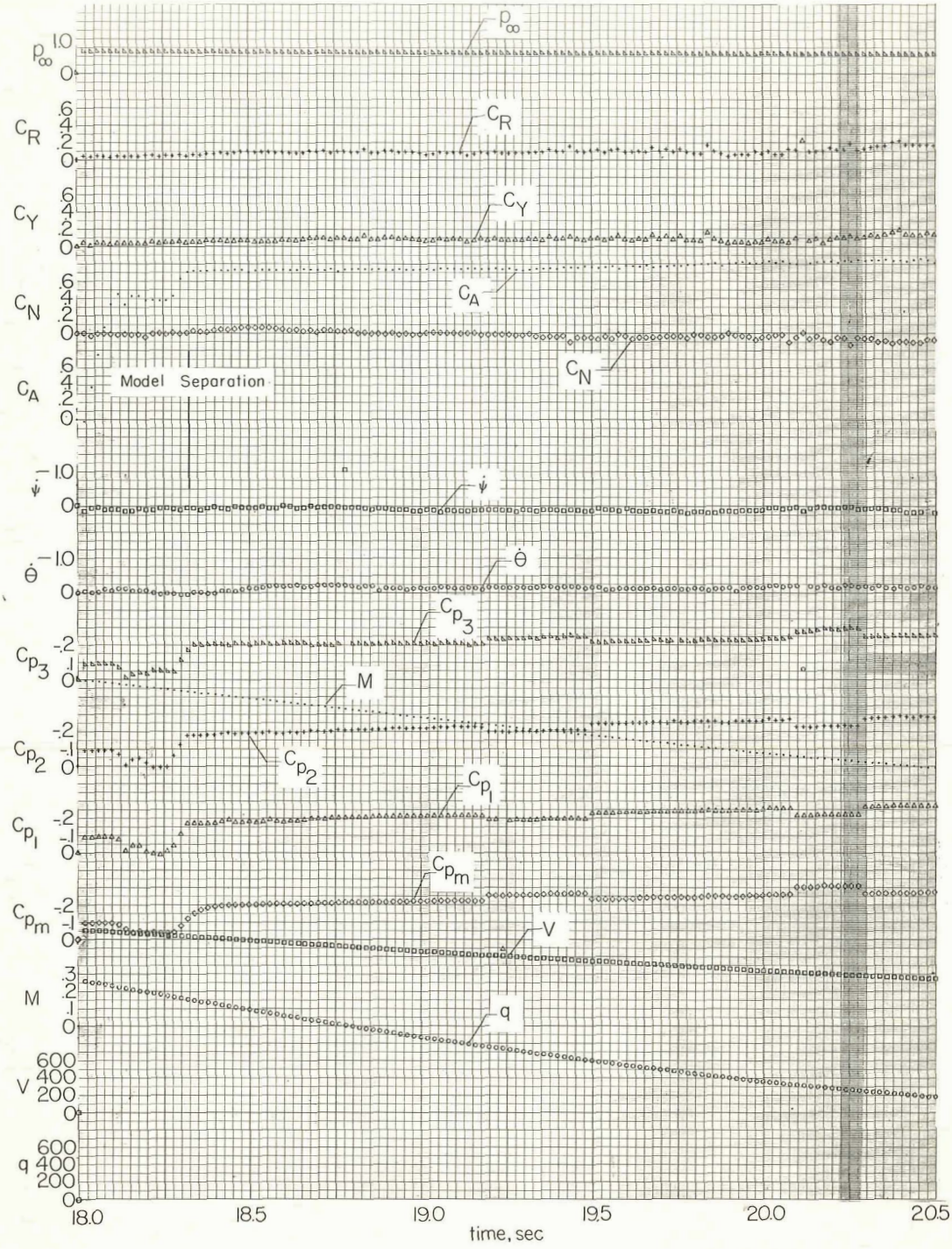

Figure 8.- Time history of free-flight data for model B.

CONFIDENTIAL

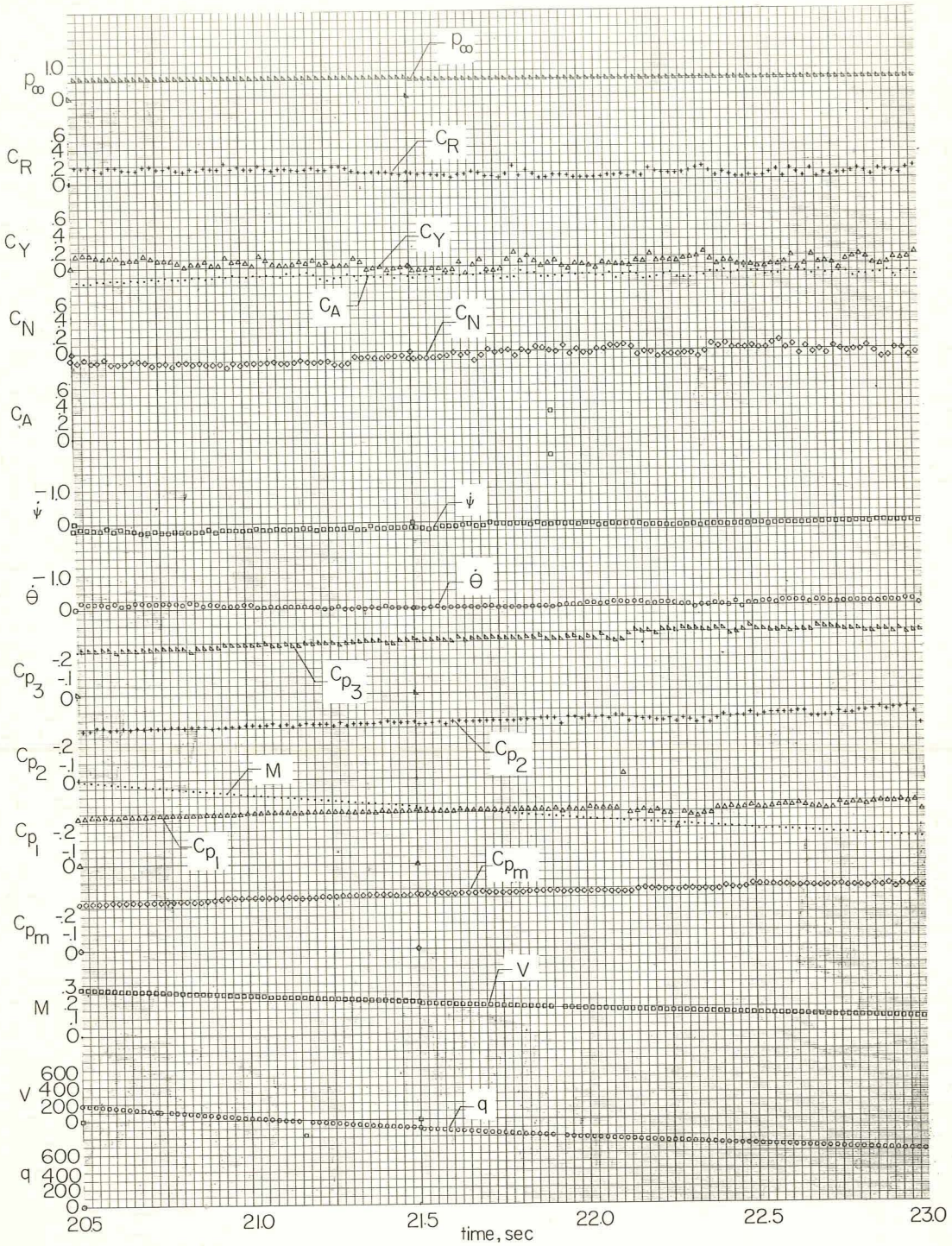

Figure 8.- Continued.

CONFIDENTIAL

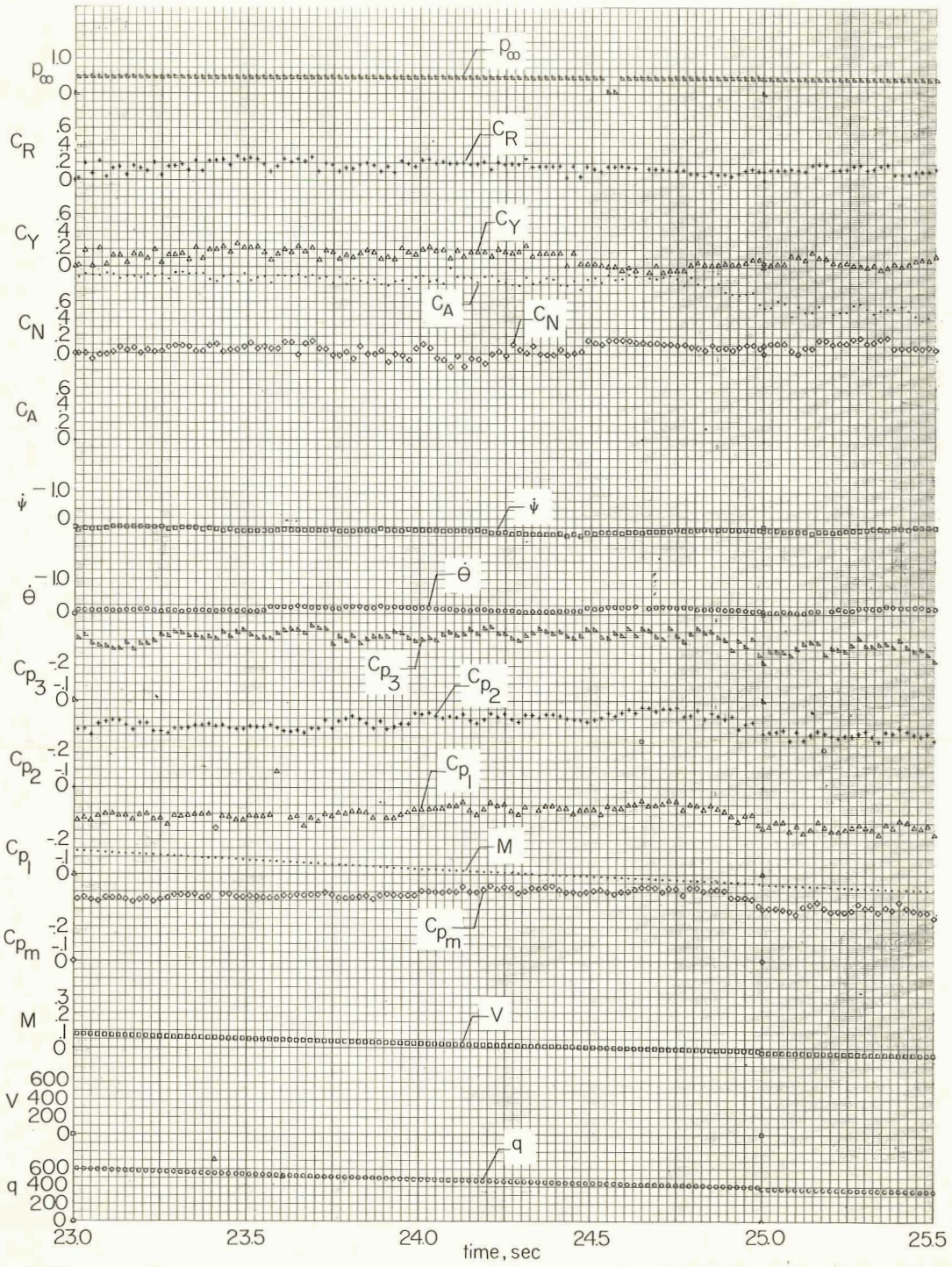

Figure 8.- Continued.

CONFIDENTIAL

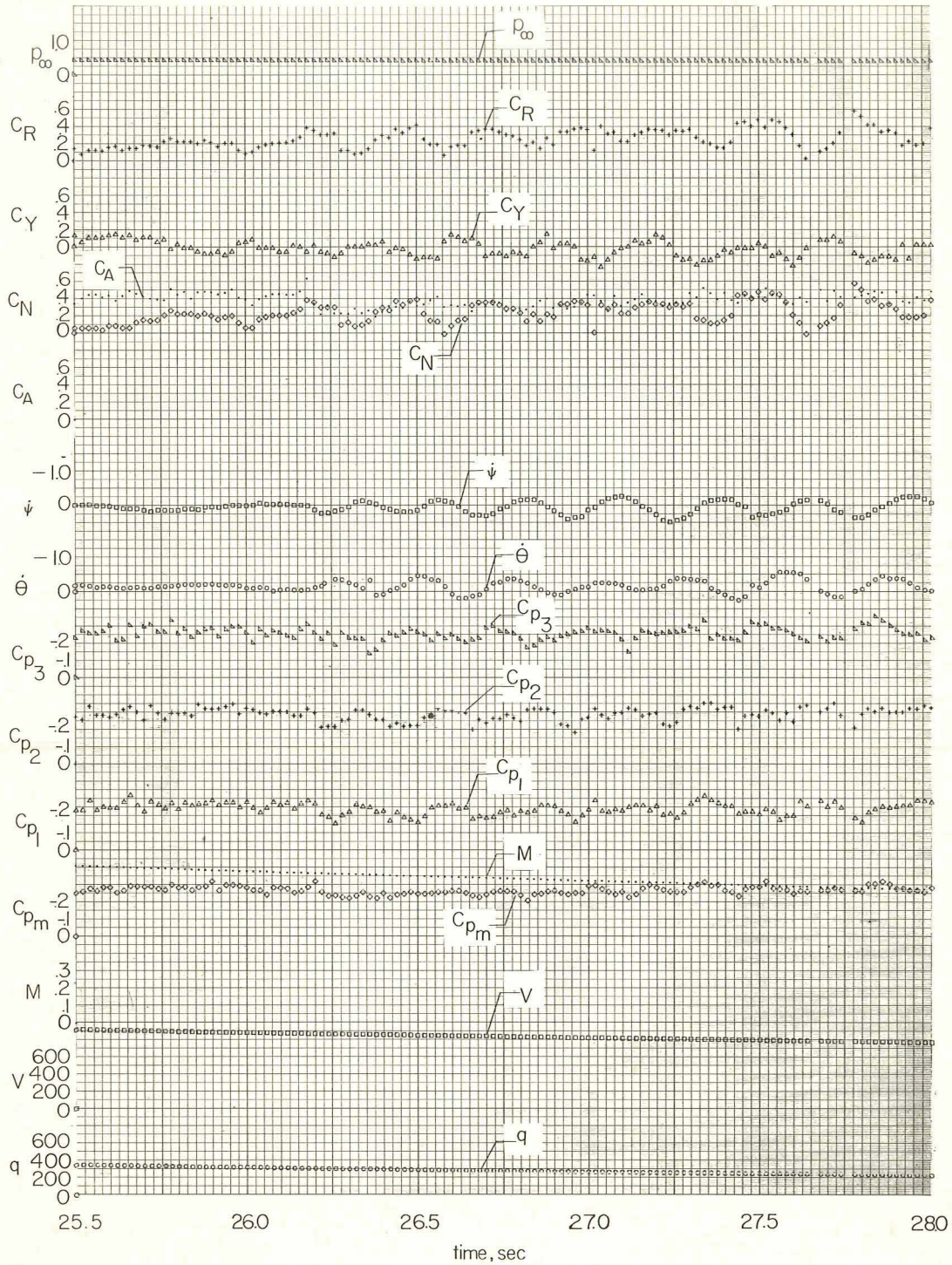

Figure 8.- Continued.

I-656

CONFIDENTIAL

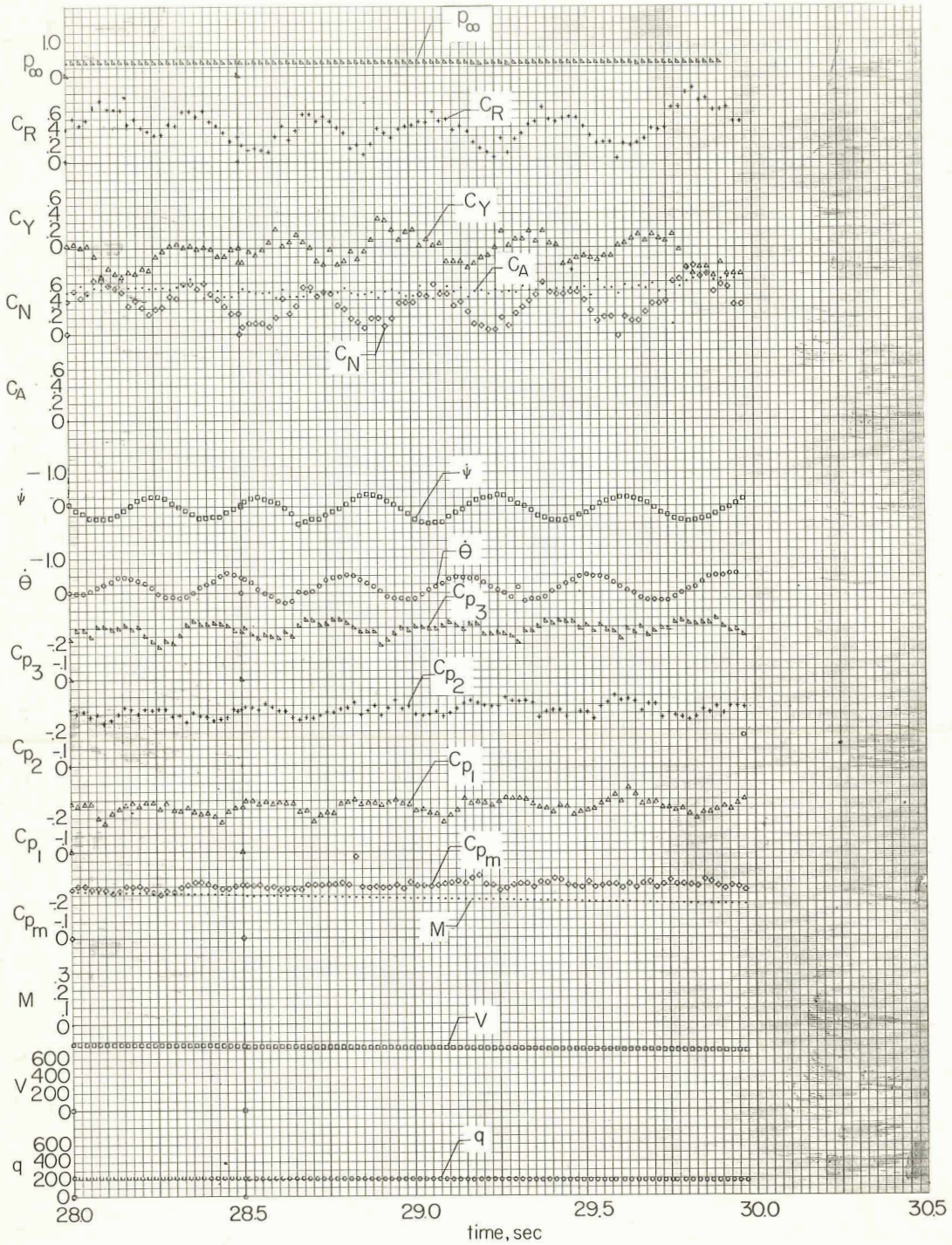

Figure 8.- Concluded.

CONFIDENTIAL

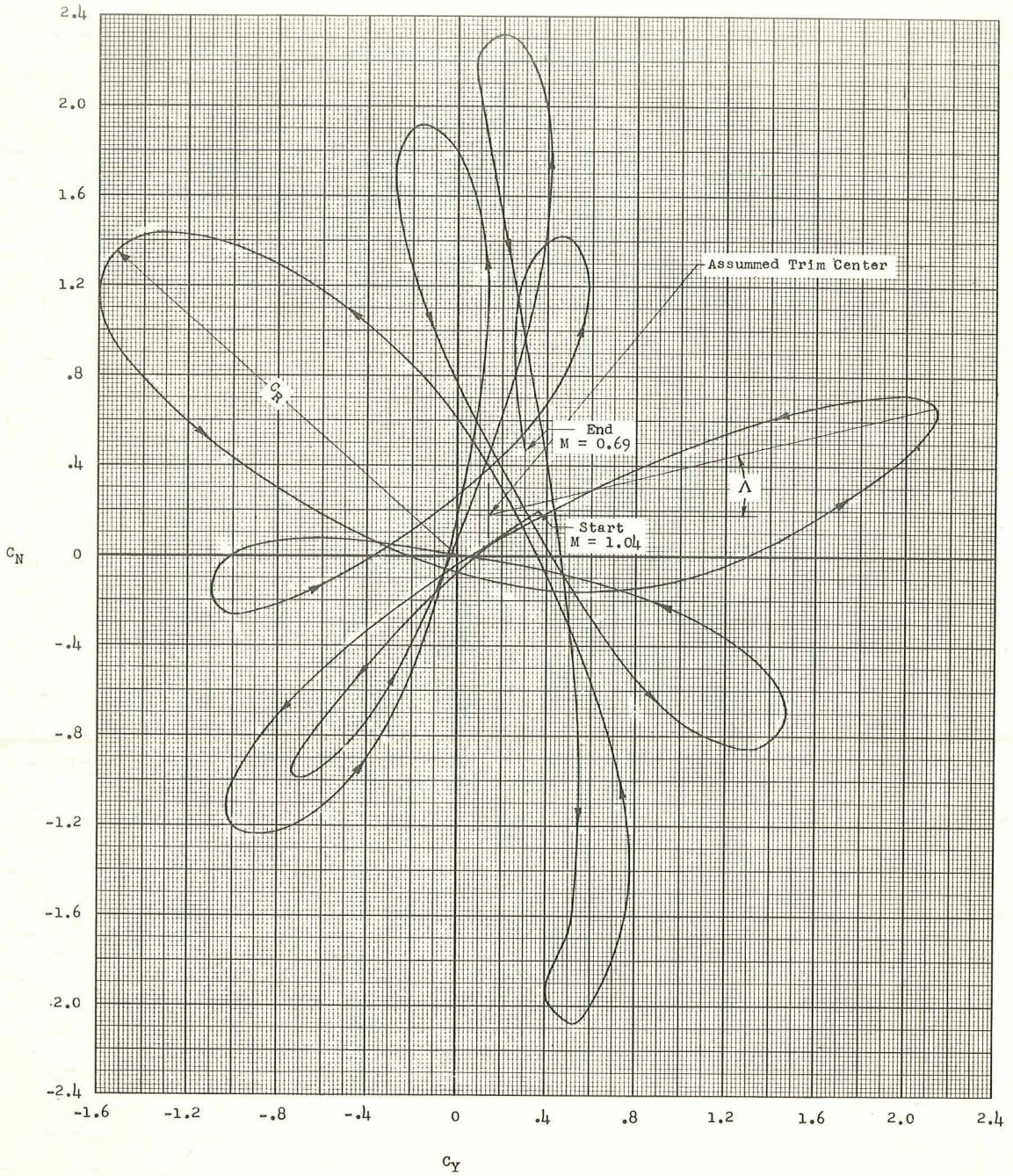

Figure 9.- Plot of the normal- and transverse-force coefficients for model A. Increasing time is indicated by the arrows.

I-656

CONFIDENTIAL

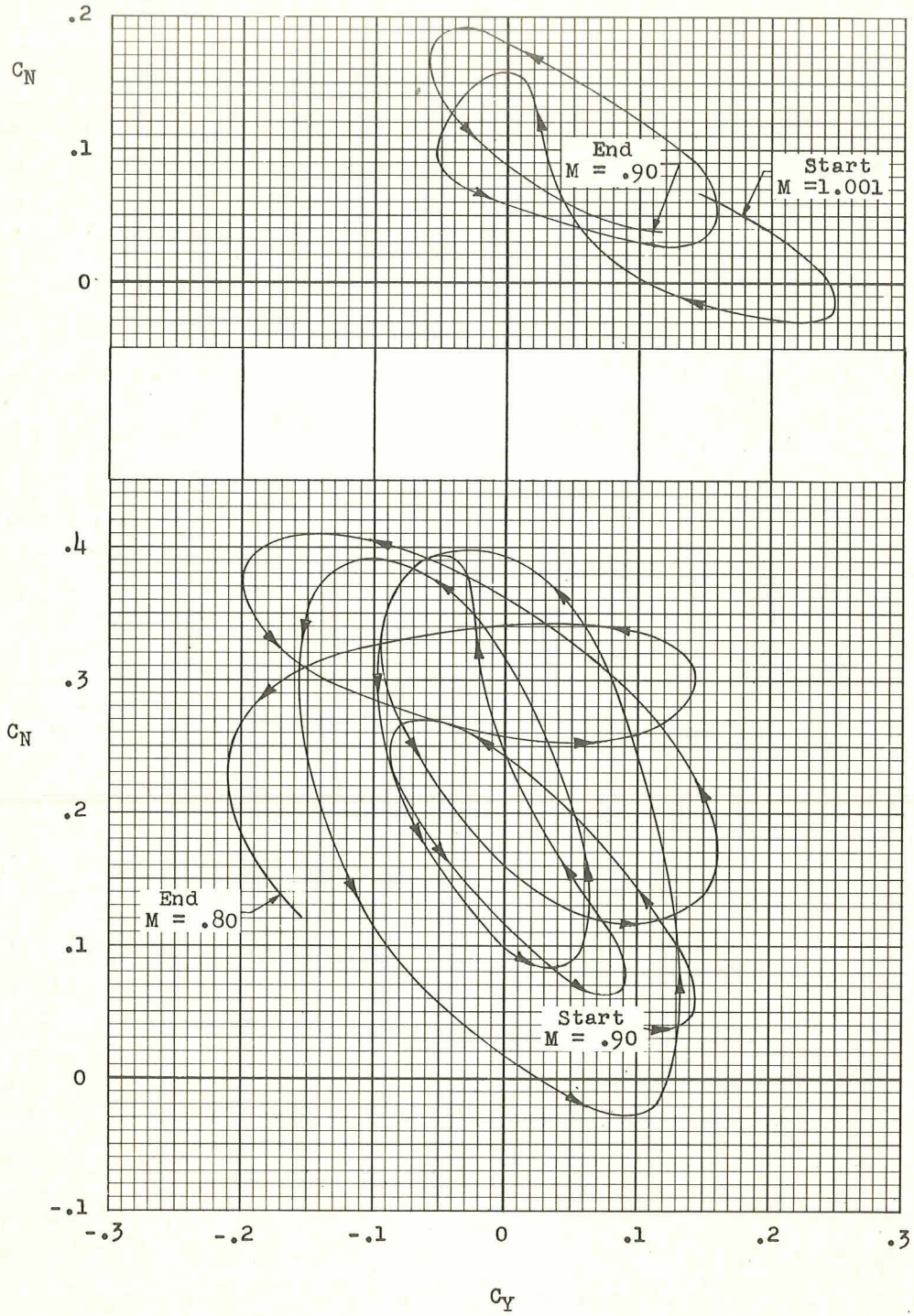

Figure 10.- Plot of the normal- and transverse-force coefficients for model B. Increasing time is indicated by the arrows.

CONFIDENTIAL

L-656

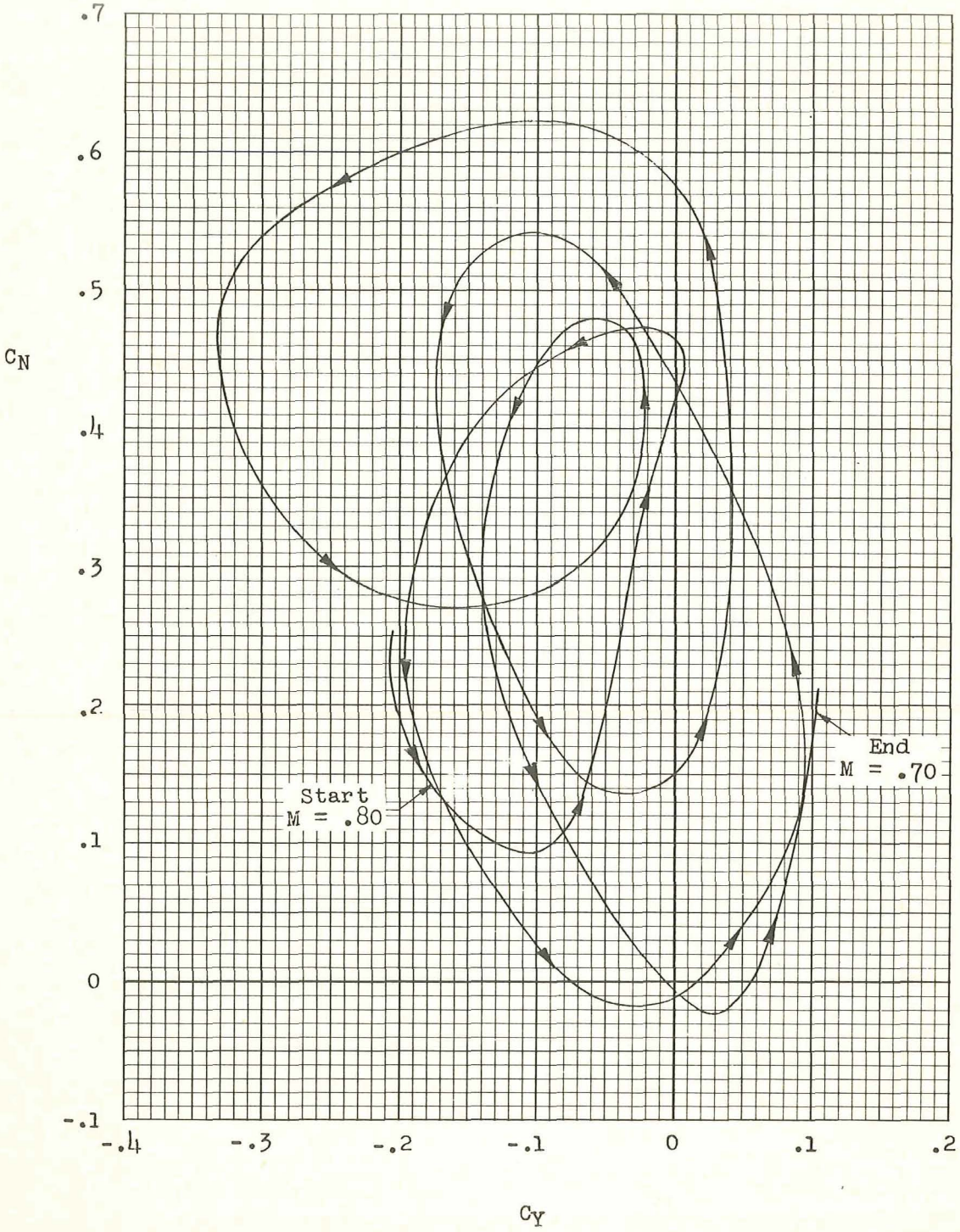

Figure 10.- Concluded.

L-656

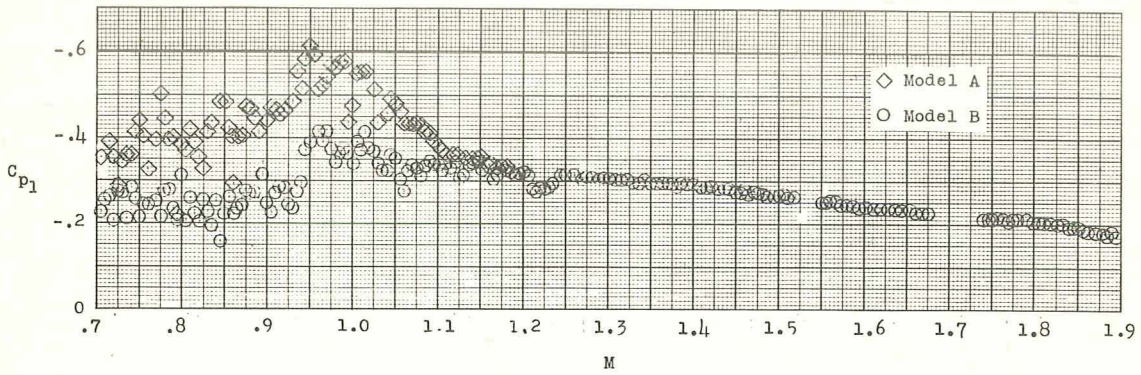

(a) Base pressure coefficients at station 1.

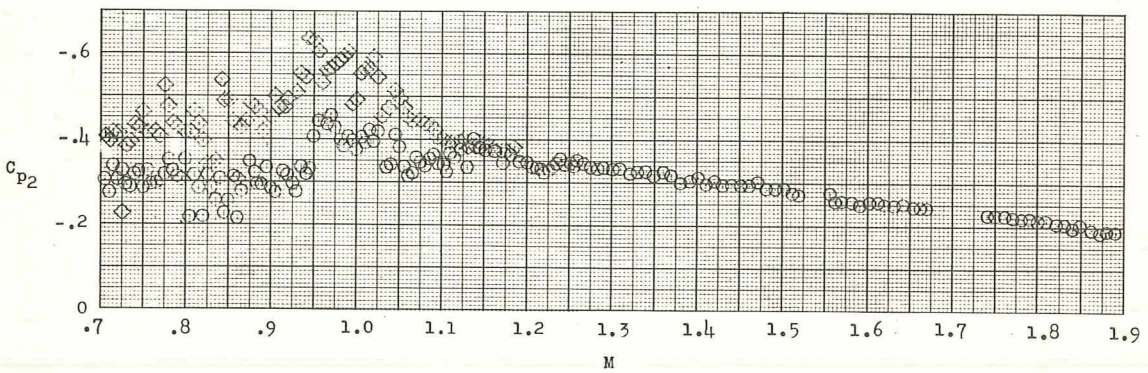

(b) Base pressure coefficients at station 2.

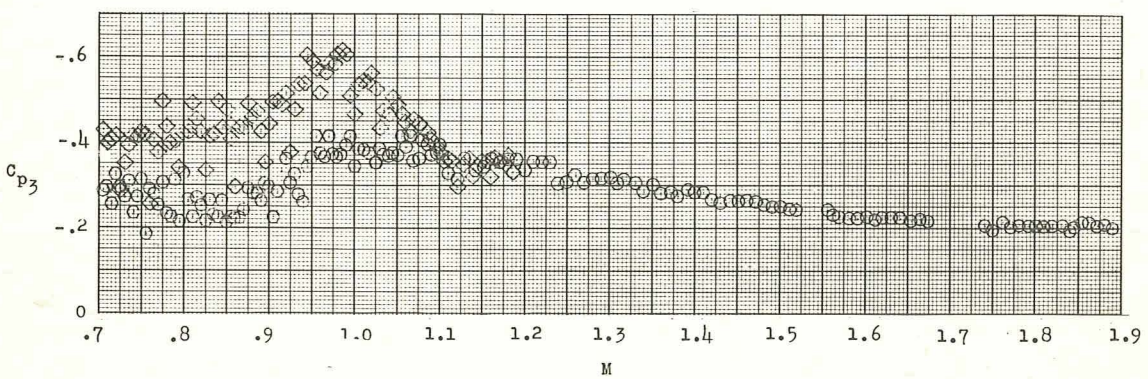

(c) Base pressure coefficients at station 3.

Figure 11.- Variation of the measured base pressure coefficients with Mach number for models A and B.

CONFIDENTIAL

I-956

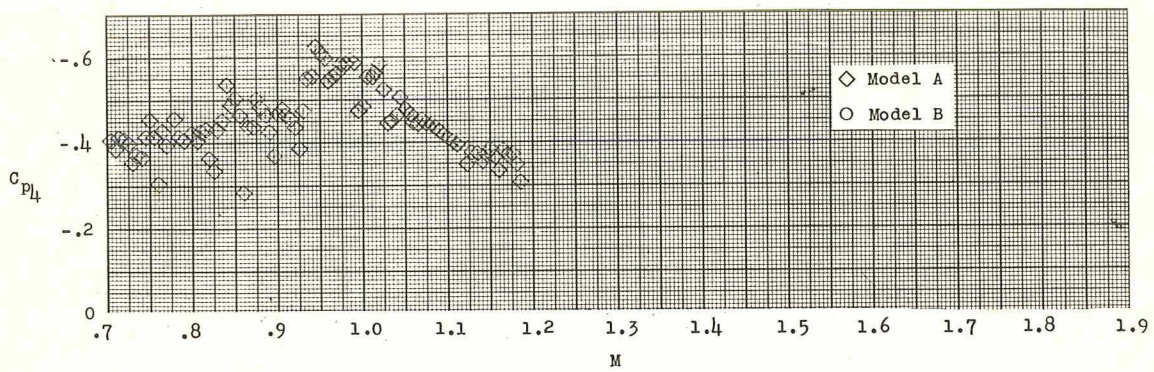

(d) Base pressure coefficients at station 4.

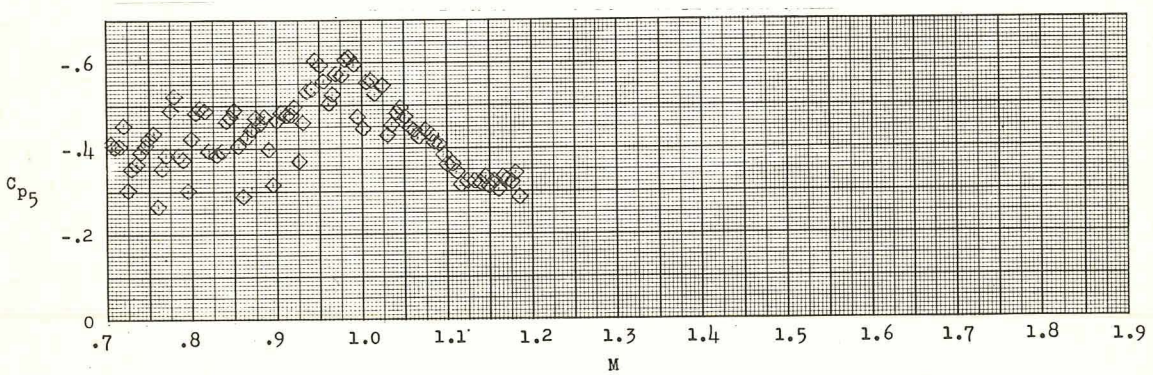

(e) Base pressure coefficients at station 5.

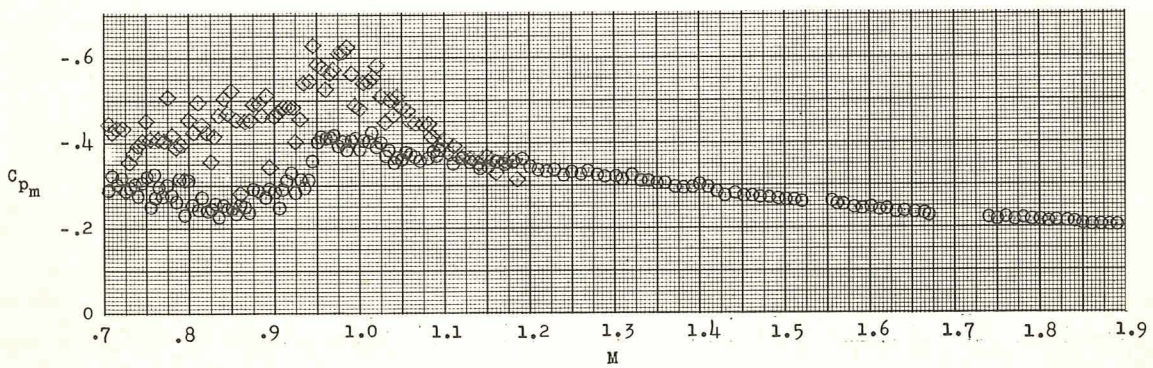

(f) Manifold base pressure coefficients.

Figure 11.- Concluded.

CONFIDENTIAL

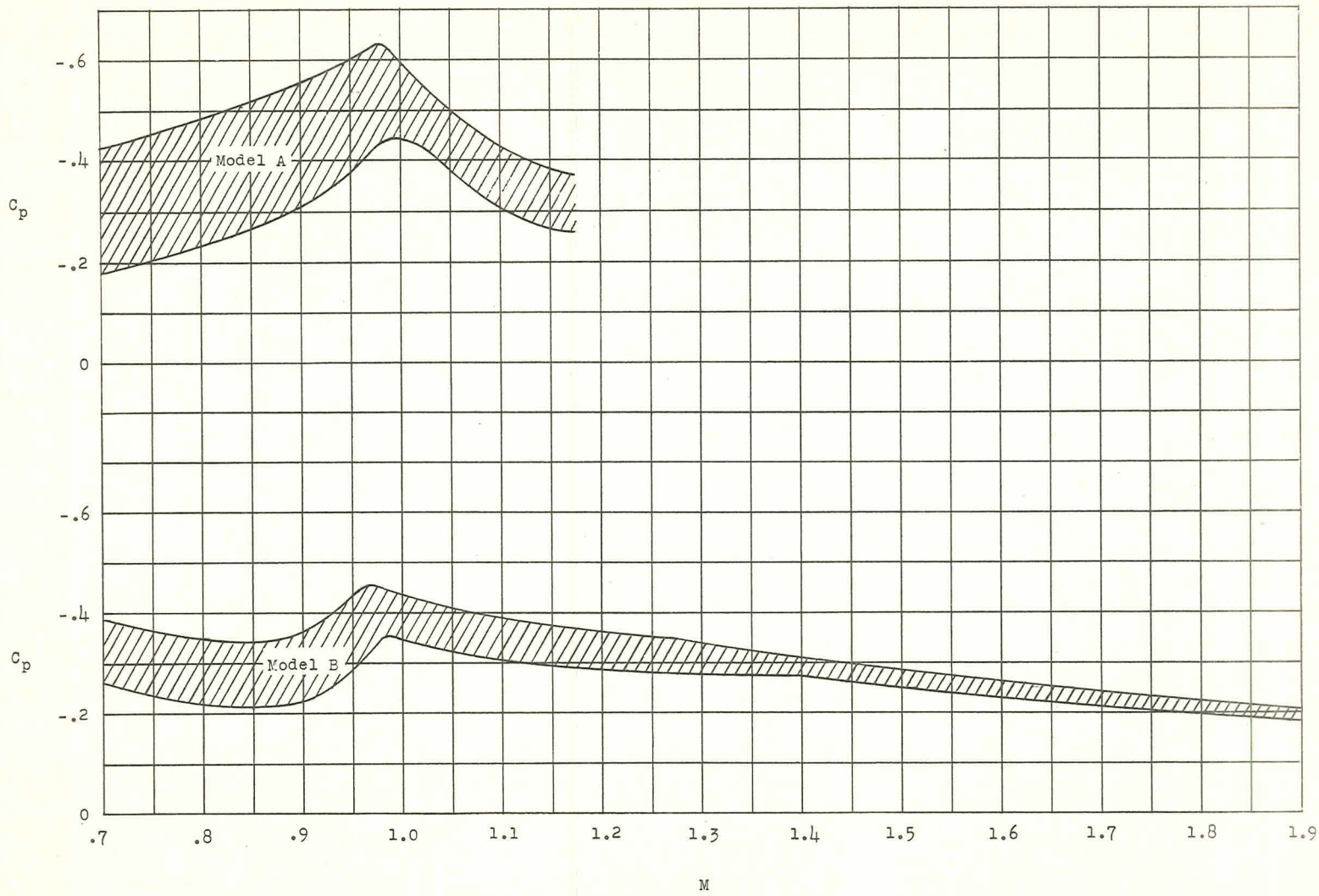

Figure 12.- Envelope of the measured base pressure coefficients for models A and B.

CONFIDENTIAL

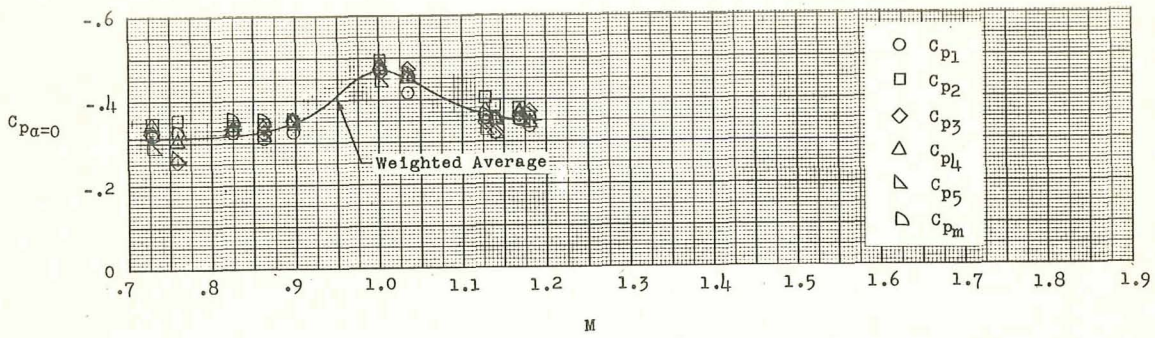

(a) Base pressure coefficients at approximately zero angle of attack for model A.

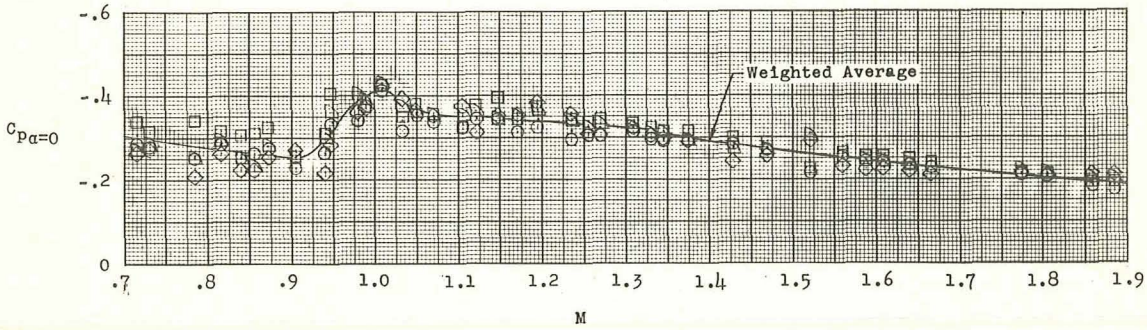

(b) Base pressure coefficients at approximately zero angle of attack for model B.

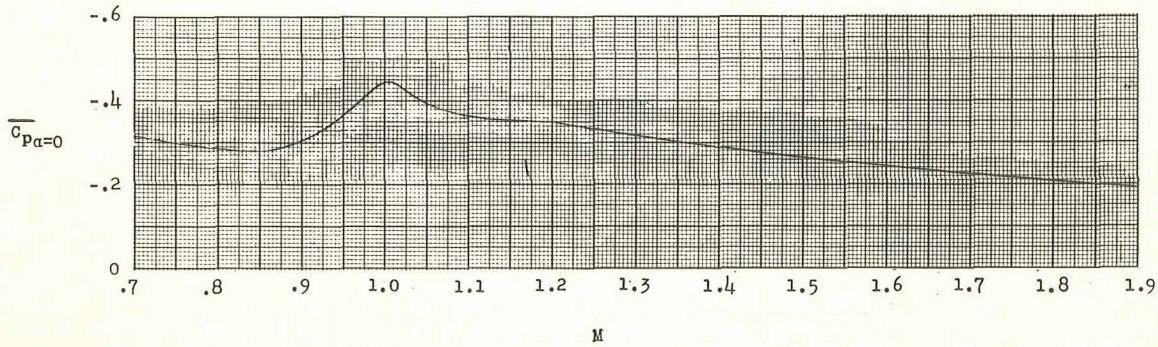

(c) Average base pressure coefficients at approximately zero angle of attack for models A and B.

Figure 13.- Variation of the average base pressure coefficients with Mach number at approximately zero angle of attack for models A and B.

L-656

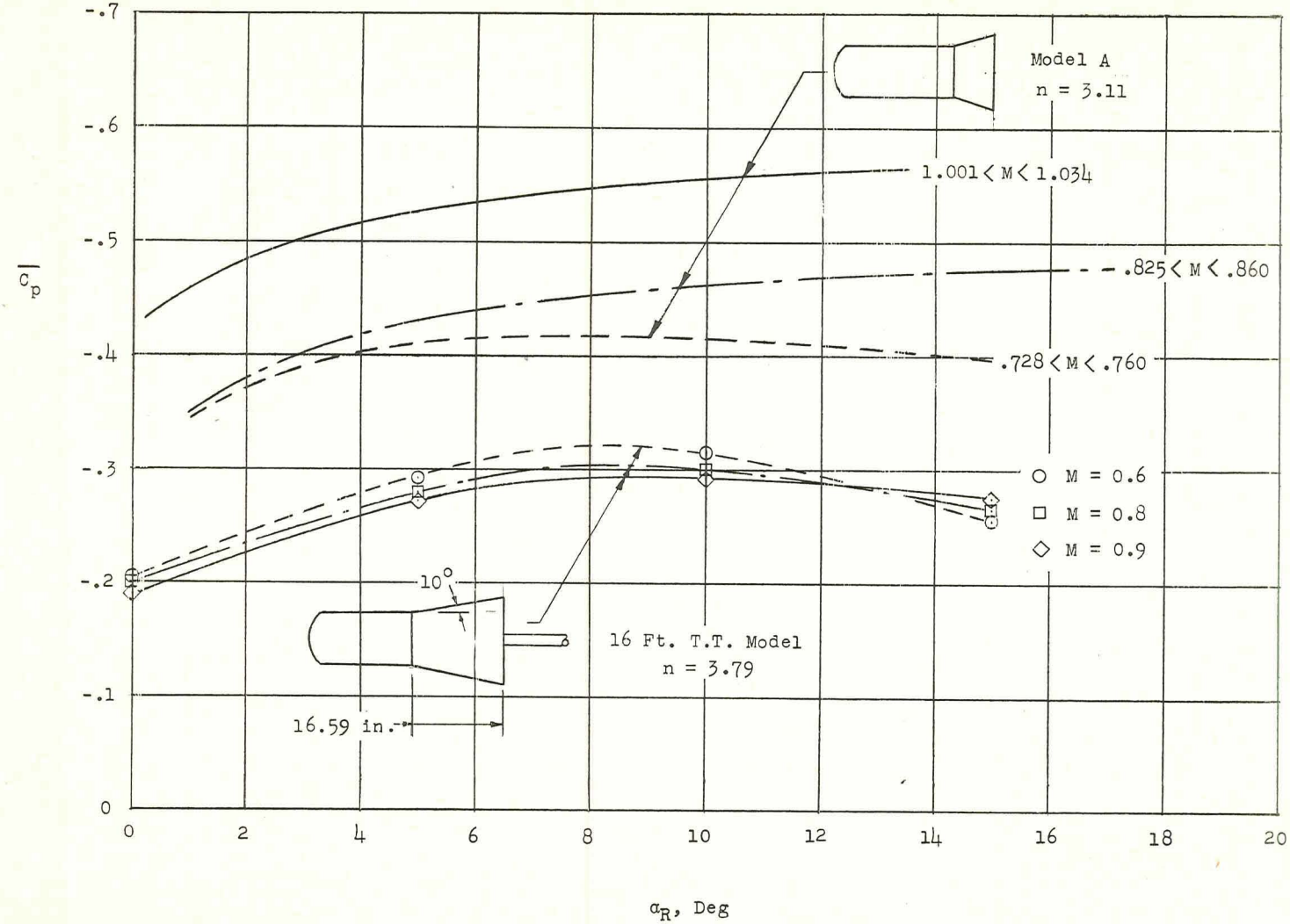

Figure 14.- Variation of the average base pressure coefficient with resultant angle of attack for model A.

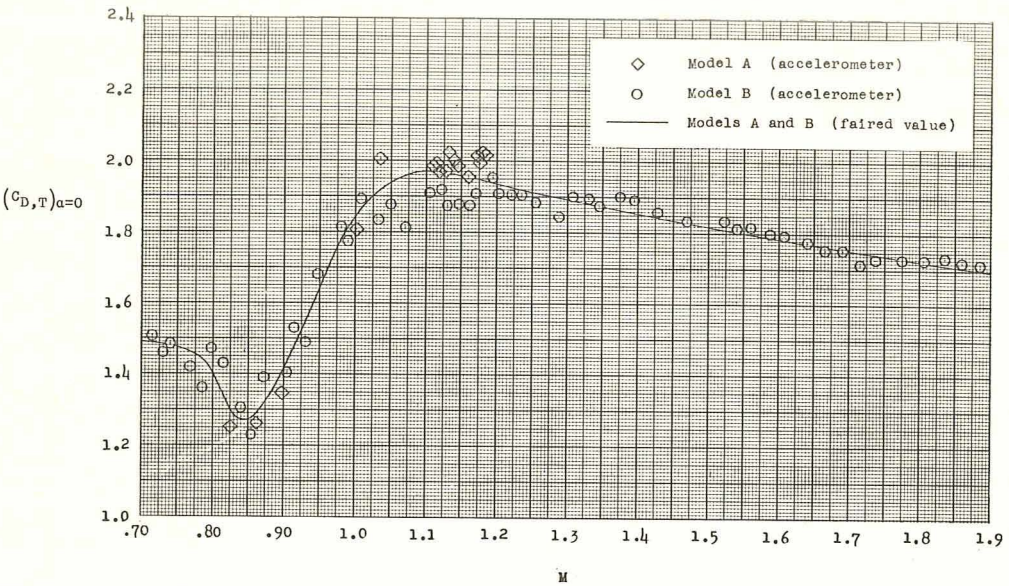

(a) Total drag coefficient at approximately zero angle of attack.

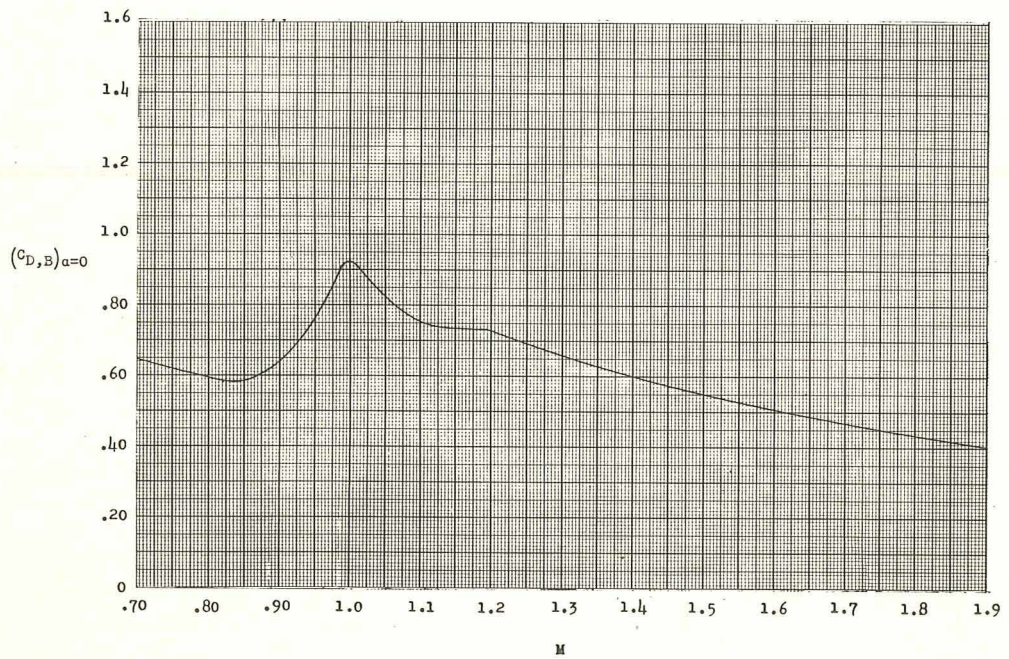

(b) Base drag coefficient at approximately zero angle of attack.

Figure 15.- Variation of the total and base drag coefficients with Mach number at approximately zero angle of attack for models A and B.

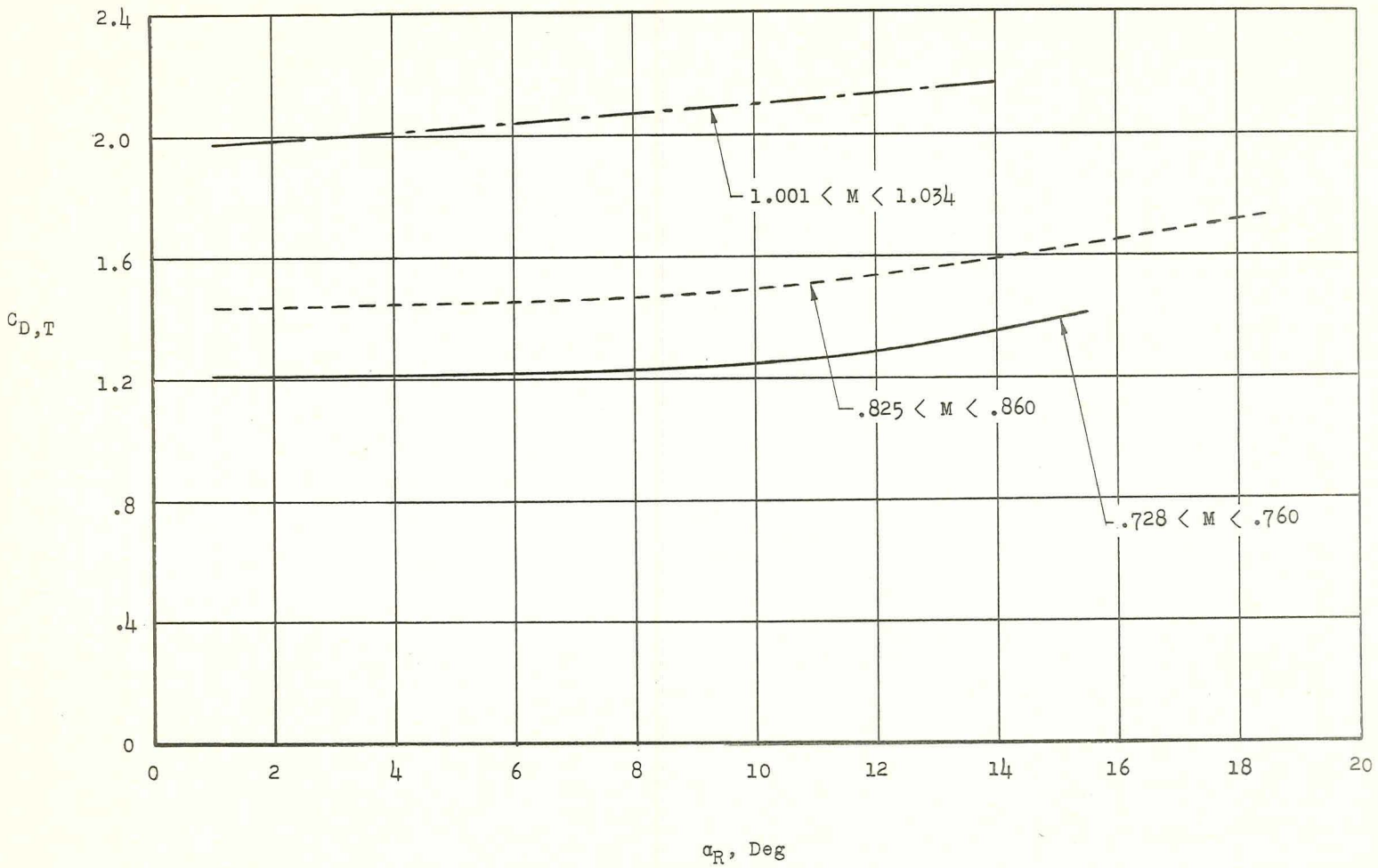

Figure 16.- Variation of the total drag coefficient with resultant angle of attack for model A.

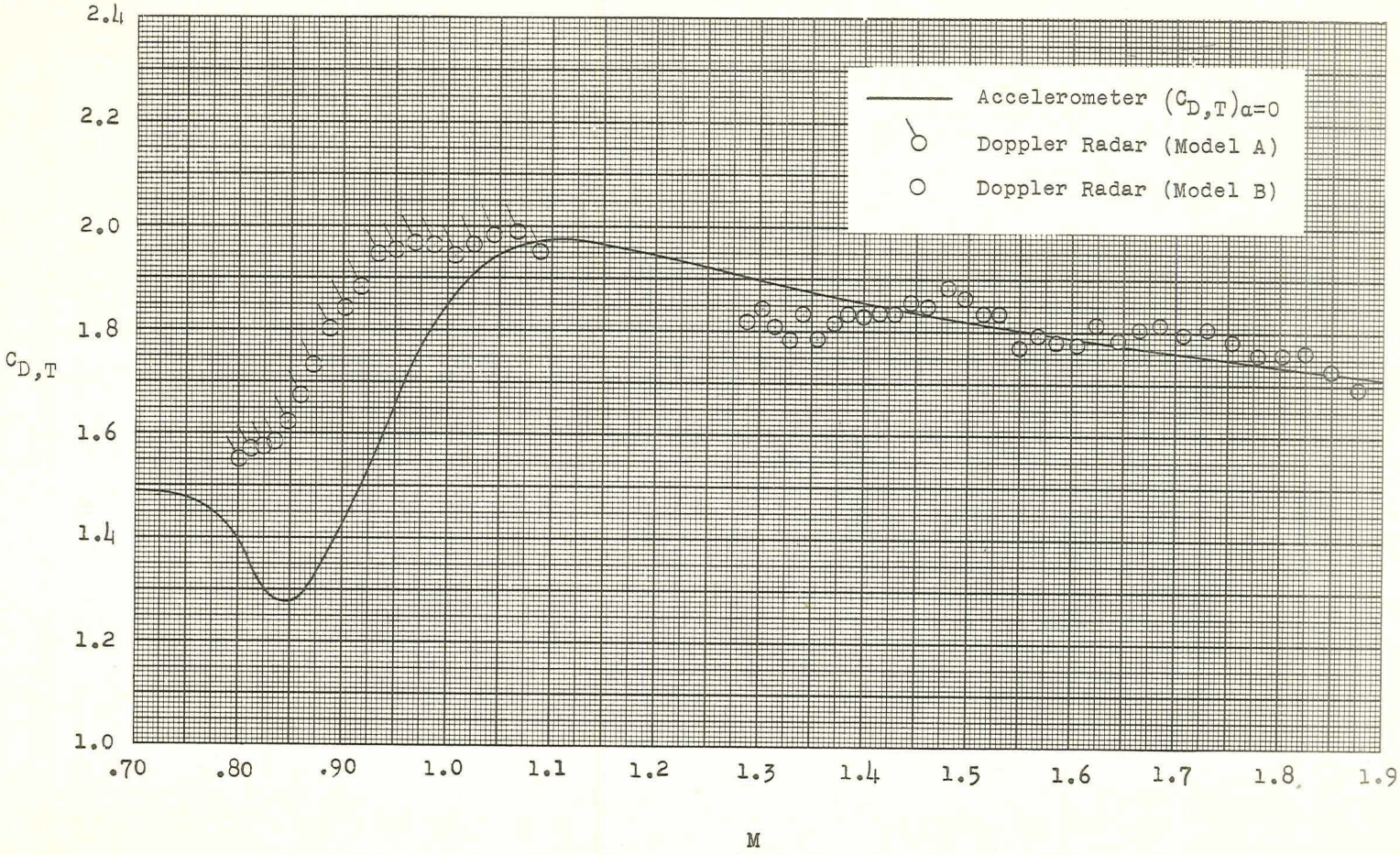

Figure 17.- Comparison of the variation of total drag coefficient of model B with Mach number at approximately zero angle of attack.

CONFIDENTIAL

CONFIDENTIAL

CONFIDENTIAL